DIII-D research advancing the physics basis for optimizing the tokamak approach to fusion energy

Fenstermacher, M. E., for the DIII-D Team

PAPER • OPEN ACCESS

DIII-D research advancing the physics basis for optimizing the tokamak approach to fusion energy

View the article online for updates and enhancements.

DIII-D research advancing the physics basis for optimizing the tokamak approach to fusion energy

M. E. Fenstermacher[1,*] for the DIII-D Team: J. Abbate[2], S. Abe[3],
T. Abrams[4], M. Adams[4], B. Adamson[4], N. Aiba[5], T. Akiyama[4],
P. Aleynikov[6], E. Allen[4], S. Allen[1], H. Anand[4], J. Anderson[4], Y. Andrew[7],
T. Andrews[4], D. Appelt[4], R. Arbon[3], N. Ashikawa[8], A. Ashourvan[2],
M. Aslin[9], Y. Asnis[10], M. Austin[11], D. Ayala[4], J. Bak[12],
I. Bandyopadhyay[13], S. Banerjee[14], K. Barada[15], L. Bardoczi[4], J. Barr[4],
E. Bass[16], D. Battaglia[2], A. Battey[17], W. Baumgartner[18], L. Baylor[19],
J. Beckers[20], M. Beidler[19], E. Belli[4], J. Berkery[17], T. Bernard[21],
N. Bertelli[2], M. Beurskens[6], R. Bielajew[18], S. Bilgili[22], B. Biswas[18],
S. Blondel[23], J. Boedo[16], I. Bogatu[24], R. Boivin[4], T. Bolzonella[25],
M. Bongard[26], X. Bonnin[27], P. Bonoli[18], M. Bonotto[25], A. Bortolon[2],
S. Bose[3], N. Bosviel[28], S. Bouwmans[20], M. Boyer[2], W. Boyes[17],
L. Bradley[15], R. Brambila[4], D. Brennan[3], S. Bringuier[4], L. Brodsky[4],
M. Brookman[4], J. Brooks[29], D. Brower[15], G. Brown[1], W. Brown[2],
M. Burke[26], K. Burrell[4], K. Butler[23], R. Buttery[4], I. Bykov[16], P. Byrne[4],
A. Cacheris[23], K. Callahan[15], J. Callen[26], G. Campbell[4], J. Candy[4],
J. Canik[19], P. Cano-Megias[30], N. Cao[18], L. Carayannopoulos[18],
T. Carlstrom[4], W. Carrig[4], T. Carter[15], W. Cary[4], L. Casali[4], M. Cengher[4],
G. Cespedes Paz[31], R. Chaban[32], V. Chan[115], B. Chapman[26], I. Char[33],
A. Chattopadhyay[34], R. Chen[35], J. Chen[35], X. Chen[4], X. Chen[18],
J. Chen[36], M. Chen[37], J. Chen[15], Z. Chen[11], M. Choi[12], W. Choi[3], G. Choi[38],
L. Chousal[16], C. Chrobak[39], C. Chrystal[4], Y. Chung[33], R. Churchill[2],
M. Cianciosa[19], J. Clark[40], M. Clement[2], S. Coda[41], A. Cole[42], C. Collins[19],
W. Conlin[3], A. Cooper[41], J. Cordell[2], B. Coriton[4], T. Cote[26], J. Cothran[43],
A. Creely[18], N. Crocker[15], C. Crowe[4], B. Crowley[4], T. Crowley[44],
D. Cruz-Zabala[30], D. Cummings[4], M. Curie[11], D. Curreli[45], A. Dal Molin[46],
B. Dannels[19], A. Dautt-Silva[4], K. Davda[23], G. De Tommasi[47], P. De Vries[27],
G. Degrandchamp[38], J. Degrassie[4], D. Demers[44], S. Denk[18],
S. Depasquale[2], E. Deshazer[48], A. Diallo[2], S. Diem[26], A. Dimits[1],
R. Ding[35], S. Ding[21], W. Ding[15], T. Do[16], J. Doane[4], G. Dong[2],
D. Donovan[23], J. Drake[4], W. Drews[4], J. Drobny[45], X. Du[4], H. Du[49],
V. Duarte[2], D. Dudt[3], C. Dunn[48], J. Duran[23], A. Dvorak[19], F. Effenberg[2],
N. Eidietis[4], D. Elder[50], D. Eldon[4], R. Ellis[2], W. Elwasif[19], D. Ennis[51],
K. Erickson[2], D. Ernst[18], M. Fasciana[52], D. Fedorov[21], E. Feibush[2],
N. Ferraro[2], J. Ferreira[53], J. Ferron[4], P. Fimognari[44], D. Finkenthal[54],
R. Fitzpatrick[11], P. Fox[55], W. Fox[2], L. Frassinetti[56], H. Frerichs[26],
H. Frye[57], Y. Fu[3], K. Gage[38], J. Galdon Quiroga[6], A. Gallo[21], Q. Gao[49],
A. Garcia[38], M. Garcia Munoz[30], D. Garnier[18], A. Garofalo[4], A. Gattuso[4],
D. Geng[4], K. Gentle[11], D. Ghosh[1], L. Giacomelli[58], S. Gibson[59],

* Author to whom any correspondence should be addressed.

E. Gilson[2], C. Giroud[55], F. Glass[4], A. Glasser[3], D. Glibert[4], P. Gohil[4],
R. Gomez[4], S. Gomez[4], X. Gong[35], E. Gonzales[4], A. Goodman[3],
Y. Gorelov[4], V. Graber[60], R. Granetz[18], T. Gray[19], D. Green[19],
C. Greenfield[4], M. Greenwald[18], B. Grierson[2] ⓘ, R. Groebner[4],
W. Grosnickle[4], M. Groth[61], H. Grunloh[4], S. Gu[21], W. Guo[35], H. Guo[4],
P. Gupta[4], J. Guterl[4], W. Guttenfelder[2], T. Guzman[4], S. Haar[4], R. Hager[2],
S. Hahn[12], M. Halfmoon[11], T. Hall[4], K. Hallatschek[6], F. Halpern[4],
G. Hammett[2], H. Han[62], E. Hansen[38], C. Hansen[63], M. Hansink[4],
J. Hanson[17], M. Hanson[16], G. Hao[49], A. Harris[4], R. Harvey[64], S. Haskey[2],
E. Hassan[11], A. Hassanein[29], D. Hatch[11], R. Hawryluk[2], W. Hayashi[38],
W. Heidbrink[38], J. Herfindal[19], J. Hicok[4], D. Hill[4], E. Hinson[26],
C. Holcomb[1], L. Holland[4], C. Holland[16], E. Hollmann[16], J. Hollocombe[55],
A. Holm[61], I. Holmes[4], K. Holtrop[4], M. Honda[5], R. Hong[15], R. Hood[65],
A. Horton[19], L. Horvath[55], M. Hosokawa[27], S. Houshmandyar[11],
N. Howard[18], E. Howell[66], D. Hoyt[4], W. Hu[35], Y. Hu[35], Q. Hu[2] ⓘ,
J. Huang[35], Y. Huang[35], J. Hughes[18], T. Human[2], D. Humphreys[4],
P. Huynh[4], A. Hyatt[4], C. Ibanez[4], L. Ibarra[4], R. Icasas[4], K. Ida[8],
V. Igochine[6], Y. In[67], S. Inoue[5], A. Isayama[5], O. Izacard[3], V. Izzo[4],
A. Jackson[55], G. Jacobsen[4], A. Jaervinen[61], A. Jalalvand[68],
J. Janhunen[11], S. Jardin[2], H. Jarleblad[69], Y. Jeon[12], H. Ji[3], X. Jian[16],
E. Joffrin[70], A. Johansen[63], C. Johnson[51], T. Johnson[71], C. Jones[16],
I. Joseph[1], D. Jubas[3], B. Junge[4], W. Kalb[18], R. Kalling[72], C. Kamath[1],
J. Kang[12], D. Kaplan[4], A. Kaptanoglu[63], S. Kasdorf[73], J. Kates-Harbeck[74],
P. Kazantzidis[75], A. Kellman[4], D. Kellman[4], C. Kessel[19], K. Khumthong[4],
E. Kim[76], H. Kim[77], J. Kim[24], S. Kim[27], J. Kim[12], H. Kim[12], K. Kim[19],
C. Kim[78], W. Kimura[79], M. King[4], J. King[66], J. Kinsey[64], A. Kirk[55],
B. Kiyan[3], A. Kleiner[2], V. Klevarova[68], R. Knapp[4], M. Knolker[21], W. Ko[12],
T. Kobayashi[8], E. Koch[4], M. Kochan[55], B. Koel[3], M. Koepke[22], A. Kohn[80],
R. Kolasinski[65], E. Kolemen[2], E. Kostadinova[81], M. Kostuk[4], G. Kramer[2],
D. Kriete[26], L. Kripner[82], S. Kubota[15], J. Kulchar[4], K. Kwon[67], R. La Haye[4],
F. Laggner[2], H. Lan[35], R. Lantsov[15], L. Lao[4], A. Lasa Esquisabel[23],
C. Lasnier[1], C. Lau[19], B. Leard[60], J. Lee[83], R. Lee[4], M. Lee[84], M. Lee[12],
Y. Lee[12], C. Lee[85], J. Lee[85], S. Lee[23], M. Lehnen[27], A. Leonard[4],
E. Leppink[18], M. Lesher[4], J. Lestz[38], J. Leuer[4], N. Leuthold[6], X. Li[35],
K. Li[35], E. Li[35], G. Li[35], L. Li[86], Z. Li[21], J. Li[49], Y. Li[87], Z. Lin[38], D. Lin[38],
X. Liu[35], J. Liu[35], Y. Liu[35], T. Liu[88], Y. Liu[4], C. Liu[4], Z. Liu[48], C. Liu[2],
D. Liu[3], A. Liu[3], D. Liu[38], A. Loarte-Prieto[27], L. Lodestro[1], N. Logan[1],
J. Lohr[4], B. Lombardo[4], J. Lore[19], Q. Luan[88], T. Luce[27], T. Luda Di
Cortemiglia[6], N. Luhmann[37], R. Lunsford[2], Z. Luo[35], A. Lvovskiy[4],
B. Lyons[4], X. Ma[21], M. Madruga[4], B. Madsen[69], C. Maggi[55],
K. Maheshwari[89], A. Mail[4], J. Mailloux[55], R. Maingi[2], M. Major[26],
M. Makowski[90], R. Manchanda[34], C. Marini[21], A. Marinoni[18], A. Maris[18],
T. Markovic[82], L. Marrelli[25], E. Martin[19], J. Mateja[29], G. Matsunaga[5],
R. Maurizio[21], P. Mauzey[4], D. Mauzey[2], G. Mcardle[55], J. Mcclenaghan[4],
K. Mccollam[26], C. Mcdevitt[91], K. Mckay[14], G. Mckee[26], A. Mclean[1],
V. Mehta[33], E. Meier[92], J. Menard[2], O. Meneghini[4], G. Merlo[11],
S. Messer[23], W. Meyer[1], C. Michael[15], C. Michoski[93], P. Milne[94], G. Minet[4],
A. Misleh[2], Y. Mitrishkin[95], C. Moeller[4], K. Montes[18], M. Morales[96],
S. Mordijck[32], D. Moreau[70], S. Morosohk[60], P. Morris[4], L. Morton[26],
A. Moser[4], R. Moyer[16], C. Moynihan[45], T. Mrazkova[97], D. Mueller[2],
S. Munaretto[4], J. Munoz Burgos[98], C. Murphy[4], K. Murphy[99],
C. Muscatello[4], C. Myers[65], A. Nagy[2], G. Nandipati[100], M. Navarro[26],
F. Nave[53], G. Navratil[17], R. Nazikian[2], A. Neff[101], G. Neilson[2], T. Neiser[21],

W. Neiswanger[33], D. Nelson[4], A. Nelson[3], F. Nespoli[2], R. Nguyen[4],
L. Nguyen[102], X. Nguyen[15], J. Nichols[23], M. Nocente[46], S. Nogami[22],
S. Noraky[4], N. Norausky[4], M. Nornberg[26], R. Nygren[65], T. Odstrcil[4],
D. Ogas[4], T. Ogorman[4], S. Ohdachi[8], Y. Ohtani[5], M. Okabayashi[2],
M. Okamoto[103], L. Olavson[104], E. Olofsson[4], M. Omullane[105], R. Oneill[4],
D. Orlov[16], W. Orvis[1], T. Osborne[4], D. Pace[4], G. Paganini Canal[10],
A. Pajares Martinez[60], L. Palacios[2], C. Pan[35], Q. Pan[18], R. Pandit[14],
M. Pandya[26], A. Pankin[2], Y. Park[17], J. Park[19], J. Park[2], S. Parker[73],
P. Parks[4], M. Parsons[106], B. Patel[87], C. Pawley[4], C. Paz-Soldan[4],
W. Peebles[15], S. Pelton[21], R. Perillo[16], C. Petty[4], Y. Peysson[70],
D. Pierce[4], A. Pigarov[64], L. Pigatto[25], D. Piglowski[4], S. Pinches[27],
R. Pinsker[4], P. Piovesan[25], N. Piper[48], A. Pironti[47], R. Pitts[27], J. Pizzo[107],
U. Plank[6], M. Podesta[2], E. Poli[6], F. Poli[2], D. Ponce[4], Z. Popovic[16],
M. Porkolab[18], G. Porter[90], C. Powers[108], S. Powers[108], R. Prater[4],
Q. Pratt[15], I. Pusztai[109], J. Qian[35], X. Qin[26], O. Ra[67], T. Rafiq[60], T. Raines[2],
R. Raman[63], J. Rauch[4], A. Raymond[4], C. Rea[18], M. Reich[6], A. Reiman[2],
S. Reinhold[4], M. Reinke[19], R. Reksoatmodjo[14], Q. Ren[35], Y. Ren[2],
J. Ren[23], M. Rensink[1], J. Renteria[4], T. Rhodes[15], J. Rice[18], R. Roberts[4],
J. Robinson[110], P. Rodriguez Fernandez[18], T. Rognlien[1], A. Rosenthal[18],
S. Rosiello[111], J. Rost[18], J. Roveto[48], W. Rowan[11], R. Rozenblat[2],
J. Ruane[4], D. Rudakov[16], J. Ruiz Ruiz[112], R. Rupani[4], S. Saarelma[4],
S. Sabbagh[17], J. Sachdev[2], J. Saenz[4], S. Saib[89], M. Salewski[69],
A. Salmi[113], B. Sammuli[4], C. Samuell[1], A. Sandorfi[114], C. Sang[88],
J. Sarff[26], O. Sauter[41], K. Schaubel[4], L. Schmitz[15], O. Schmitz[26],
J. Schneider[33], P. Schroeder[4], K. Schultz[4], E. Schuster[60], J. Schwartz[3],
F. Sciortino[18], F. Scotti[1], J. Scoville[4], A. Seltzman[18], S. Seol[107],
I. Sfiligoi[16], M. Shafer[19], S. Sharapov[55], H. Shen[4], Z. Sheng[35], T. Shepard[4],
S. Shi[115], Y. Shibata[116], G. Shin[62], D. Shiraki[19], R. Shousha[3], H. Si[35],
P. Simmerling[117], G. Sinclair[4], J. Sinha[27], P. Sinha[2], G. Sips[4], T. Sizyuk[29],
C. Skinner[2], A. Sladkomedova[15], T. Slendebroek[21], J. Slief[20],
R. Smirnov[16], J. Smith[4], S. Smith[4], D. Smith[26], J. Snipes[27], G. Snoep[118],
A. Snyder[4], P. Snyder[4], E. Solano[119], W. Solomon[4], J. Song[120],
A. Sontag[26], V. Soukhanovskii[1], J. Spendlove[121], D. Spong[19], J. Squire[4],
C. Srinivasan[55], W. Stacey[48], G. Staebler[4], L. Stagner[21], T. Stange[6],
P. Stangeby[50], R. Stefan[4], R. Stemprok[4], D. Stephan[4], J. Stillerman[18],
T. Stoltzfus-Dueck[2], W. Stonecipher[4], S. Storment[15], E. Strait[4], D. Su[4],
L. Sugiyama[18], Y. Sun[35], P. Sun[35], Z. Sun[2], A. Sun[49], D. Sundstrom[4],
C. Sung[122], J. Sungcoco[4], W. Suttrop[6], Y. Suzuki[8], T. Suzuki[5],
A. Svyatkovskiy[3], C. Swee[26], R. Sweeney[18], C. Sweetnam[2], G. Szepesi[55],
M. Takechi[5], T. Tala[113], K. Tanaka[8], X. Tang[91], S. Tang[15], Y. Tao[35], R. Tao[4],
D. Taussig[4], T. Taylor[4], K. Teixeira[4], K. Teo[63], A. Theodorsen[123],
D. Thomas[4], K. Thome[4], A. Thorman[124], A. Thornton[55], A. Ti[35],
M. Tillack[16], N. Timchenko[125], R. Tinguely[18], R. Tompkins[4], J. Tooker[4],
A. Torrezan De Sousa[4], G. Trevisan[21], S. Tripathi[15], A. Trujillo Ochoa[126],
D. Truong[65], C. Tsui[16], F. Turco[17], A. Turnbull[4], M. Umansky[1],
E. Unterberg[19], P. Vaezi[16], P. Vail[3], J. Valdez[4], W. Valkis[16],
B. Van Compernolle[4], J. Van Galen[20], R. Van Kampen[118], M. Van Zeeland[4],
G. Verdoolaege[68], N. Vianello[25], B. Victor[1], E. Viezzer[30], S. Vincena[15],
M. Wade[19], F. Waelbroeck[11], J. Wai[3], T. Wakatsuki[5], M. Walker[4],
G. Wallace[18], R. Waltz[4], W. Wampler[65], L. Wang[35], H. Wang[35],
Y. Wang[35], H. Wang[4], Z. Wang[60], H. Wang[60], Z. Wang[2], Y. Wang[37],
G. Wang[15], S. Ward[87], M. Watkins[4], J. Watkins[65], W. Wehner[4], Y. Wei[17],
M. Weiland[6], D. Weisberg[4], A. Welander[4], A. White[18], R. White[2],

S. Wiesen[127], R. Wilcox[19], T. Wilks[18], M. Willensdorfer[6], H. Wilson[87],
A. Wingen[19], M. Wolde[4], M. Wolff[1], K. Woller[18], A. Wolz[110], H. Wong[15],
S. Woodruff[42], M. Wu[35], Y. Wu[115], S. Wukitch[18], G. Wurden[91], W. Xiao[128],
R. Xie[11], Z. Xing[3], X. Xu[1], C. Xu[2], G. Xu[115], Z. Yan[26], X. Yang[88], S. Yang[2],
T. Yokoyama[129], R. Yoneda[15], M. Yoshida[5], K. You[12], T. Younkin[23], J. Yu[4],
M. Yu[12], G. Yu[37], Q. Yuan[35], L. Zaidenberg[130], L. Zakharov[131],
A. Zamengo[4], S. Zamperini[23], M. Zarnstorff[3], E. Zeger[15], K. Zeller[4],
L. Zeng[15], M. Zerbini[132], L. Zhang[35], X. Zhang[35], R. Zhang[35], B. Zhang[35],
J. Zhang[35], J. Zhang[35], L. Zhao[24], B. Zhao[11], Y. Zheng[37], L. Zheng[11],
B. Zhu[1], J. Zhu[18], Y. Zhu[37], Y. Zhu[38], M. Zsutty[4] and M. Zuin[25]

1 Lawrence Livermore National Laboratory, United States of America
2 Princeton Plasma Physics Laboratory, United States of America
3 Princeton University, United States of America
4 General Atomics, United States of America
5 QST, Japan
6 Max-Planck Institute for Plasma Physics, Germany
7 Imperial College London, United Kingdom
8 National Institute for Fusion Science, Japan
9 Mt. Holyoke College, United States of America
10 University of Sao Paulo, Institute of Physics, Brazil
11 University of Texas, Austin, United States of America
12 National Fusion Research Institute, Japan
13 ITER-India, India
14 College of William and Mary, United States of America
15 University of California, Los Angeles, United States of America
16 University of California, San Diego, United States of America
17 Columbia University, United States of America
18 Massachusetts Institute of Technology, United States of America
19 Oak Ridge National Lab, United States of America
20 Eindhoven University of Technology, Netherlands
21 Oak Ridge Associated Universities, United States of America
22 West Virginia University, United States of America
23 University of Tennessee, Knoxville, United States of America
24 Far-Tech, Inc., United States of America
25 Consorzio RFX, Italy
26 University of Wisconsin, United States of America
27 ITER Organization, France
28 Stony Brook University (SUNY), United States of America
29 Purdue University, United States of America
30 University of Seville, Spain
31 Universidad de Ingenieria y Tecnologia, Peru
32 The College of William and Mary, United States of America
33 Carnegie Mellon University, United States of America
34 Insitute for Plasma Research, India
35 ASIPP, People's Republic of China
36 Peking University, People's Republic of China
37 University of California, Davis, United States of America
38 University of California, Irvine, United States of America
39 Commonwealth Fusion Systems, United States of America
40 University of Liverpool, United Kingdom
41 EPFL, Switzerland
42 Woodruff Scientific Incorporated, United States of America
43 Convergint Technologies, United States of America
44 Xantho Technologies, LLC, United States of America
45 University of Illinois, Urbana-Champaign, United States of America
46 Universita di Milano-Bicocca, Italy
47 CREATE Consortium, United States of America
48 Georgia Tech, United States of America
49 Southwestern Institute of Physics, People's Republic of China
50 University of Toronto, Canada

[51] Auburn University, United States of America

[52] Politecnico di Torino, Italy

[53] Instituto Superior Tecnico, Lisboa, Portugal

[54] Palomar College, United States of America

[55] CCFE, United Kingdom

[56] Kungliga Tekniska Hogskolan, Sweden

[57] San Diego State University, United States of America

[58] Istituto di Fisica del Plasma, CNR-EURATOM, Italy

[59] Durham University, United Kingdom

[60] Lehigh University, United States of America

[61] Aalto University, Finland

[62] Korea National Fusion Research Center, Republic of Korea

[63] University of Washington, United States of America

[64] CompX, United States of America

[65] Sandia National Lab, United States of America

[66] Tech-X Corporation, United States of America

[67] Ulsan National Institute of Science and Technology, People's Republic of China

[68] Ghent University, Belgium

[69] Technical University of Denmark, Denmark

[70] CEA Cadarache, France

[71] Drake University, United States of America

[72] Kalling Software, United States of America

[73] University of Colorado, Boulder, United States of America

[74] Harvard University, United States of America

[75] National Technical University of Athens, Greece

[76] Coventry University, United Kingdom

[77] EUROfusion, Belgium

[78] SLS2 Consulting, United States of America

[79] STI Optronics, Inc., United States of America

[80] University of Stuttgart, Germany

[81] Baylor University—CASPER, United States of America

[82] Institute of Plasma Physics AS CR, Czech Republic

[83] Alphawave Research, United States of America

[84] Harvey Mudd College, United States of America

[85] Seoul National University, Republic of Korea

[86] Donghua University, People's Republic of China

[87] University of York, United Kingdom

[88] Dalian University of Technology, People's Republic of China

[89] University of California, Berkeley, United States of America

[90] AKIMA Infrastructure Services, United States of America

[91] Los Alamos National Laboratory, United States of America

[92] Zap Energy Inc., United States of America

[93] Department of Energy, United States of America

[94] D-TACQ Solutions Ltd, United States of America

[95] Inst. of Control Sciences of the Russian Academy, People's Republic of China

[96] Fusion for Energy Joint Undertaking, United Kingdom

[97] Palomar Scientific Instruments, Inc, United States of America

[98] Astro Fusion Spectre LLC, United Kingdom

[99] University of British Columbia, Canada

[100] Pacific Northwest National Laboratory, United States of America

[101] ORISE, United States of America

[102] Michigan State University, United States of America

[103] Ishikawa National College of Technology, Japan

[104] Peak Technical Staffing, United States of America

[105] University of Strathclyde, United Kingdom

[106] Pennsylvania State University, United States of America

[107] Rensselaer Polytechnic Institute, United States of America

[108] University of Southern California, United States of America

[109] Chalmers University of Technology, Sweden

[110] University of Virginia, United States of America

[111] Università di Napoli Federico II, Italy

[112] Oxford University, United Kingdom

[113] VTT Technical Research Centre, Finland

[114] Jefferson Lab, United States of America
[115] University of Science and Technology of China, People's Republic of China
[116] National Institute of Technology, Gifu College, Japan
[117] University of Connecticut, United States of America
[118] DIFFER, Netherlands
[119] Ciemat, Spain
[120] Hanyang University, Republic of Korea
[121] Brigham Young University, United States of America
[122] KAIST, Republic of Korea
[123] UiT The Arctic University of Norway, Republic of Korea
[124] Australian National University, Australia
[125] RRC Kurchatov Institute, Russia
[126] Universidad Nacional de Ingenieria, Niccaragua
[127] Forschungszentrum Juelich, Germany
[128] Zhejiang University, People's Republic of China
[129] University of Tokyo, Japan
[130] University of Michigan, United States of America
[131] LiWFusion, United States of America
[132] ENEA C.R. Frascati, Italy

E-mail: fenstermacher1@llnl.gov

CrossMark

Abstract

DIII-D physics research addresses critical challenges for the operation of ITER and the next generation of fusion energy devices. This is done through a focus on innovations to provide solutions for high performance long pulse operation, coupled with fundamental plasma physics understanding and model validation, to drive scenario development by integrating high performance core and boundary plasmas. Substantial increases in off-axis current drive efficiency from an innovative top launch system for EC power, and in pressure broadening for Alfven eigenmode control from a co-/counter-I_p steerable off-axis neutral beam, all improve the prospects for optimization of future long pulse/steady state high performance tokamak operation. Fundamental studies into the modes that drive the evolution of the pedestal pressure profile and electron vs ion heat flux validate predictive models of pedestal recovery after ELMs. Understanding the physics mechanisms of ELM control and density pumpout by 3D magnetic perturbation fields leads to confident predictions for ITER and future devices. Validated modeling of high-Z shattered pellet injection for disruption mitigation, runaway electron dissipation, and techniques for disruption prediction and avoidance including machine learning, give confidence in handling disruptivity for future devices. For the non-nuclear phase of ITER, two actuators are identified to lower the L–H threshold power in hydrogen plasmas. With this physics understanding and suite of capabilities, a high poloidal beta optimized-core scenario with an internal transport barrier that projects nearly to $Q = 10$ in ITER at $\sim$8 MA was coupled to a detached divertor, and a near super H-mode optimized-pedestal scenario with co-I_p beam injection was coupled to a radiative divertor. The hybrid core scenario was achieved directly, without the need for anomalous current diffusion, using off-axis current drive actuators. Also, a controller to assess proximity to stability limits and regulate β_N in the ITER baseline scenario, based on plasma response to probing 3D fields, was demonstrated. Finally, innovative tokamak operation using a negative triangularity shape showed many attractive features for future pilot plant operation.

Keywords: DIII-D, tokamak, fusion energy, plasma physics, core–edge integration

(Some figures may appear in colour only in the online journal)

1. Introduction

The mission of the DIII-D program is to provide a physics basis for the optimization of tokamak operations for fusion energy production. This is done through a continuous process of facility enhancements, experimental studies targeting fundamental physics understanding of mechanisms critical to future fusion power plant operation, and experiments to test candidate scenarios integrating optimized core and edge plasma performance. These advances are then used to validate key physics-based models and increase confidence in the use of those models for predictions of future device performance and optimization. Recent progress in each of these areas is described below. This paper is organized as follows. Section 2 describes innovative facility and algorithm upgrades that have been used to address key aspects of core plasma performance optimization in reactor relevant regimes. Studies of selected solutions to physics issues critical to reactor operations are described in section 3. These results are brought together in studies of integrated core–edge scenarios applicable to optimized power plant operation in section 4. Conclusions and a future outlook are given in section 5.

2. Innovative solutions for high performance long pulse operation

Experiments using recent hardware upgrades in DIII-D contribute to providing the physics basis for optimizing future steady state tokamak performance. In particular, upgrades to the neutral beam injection (NBI) and electron cyclotron heating (ECH) systems have allowed experiments to achieve greater control of the current and pressure profiles to improve performance and stability. The off-axis NBI power in DIII-D was increased by a factor of $\sim$2, increasing both the off-axis pressure and current density for advanced tokamak (AT) scenarios. By launching from a higher poloidal angle with a nearly vertical beam trajectory in the poloidal plane projection, 'top launch' off-axis EC current drive efficiency was doubled. Additional high-density off-axis wave heating and current drive can be provided by a high harmonic fast wave (HHFW) helicon system. Detailed results will be given below.

The new and unique co-/counter-I_p steerable off-axis neutral beam [1] recently installed in DIII-D improves performance of steady state tokamak scenarios by reducing losses of energetic beam ions due to various instabilities [2]. Successful creation of a high-q_{min} steady state scenario in the ITER fusion power operation (FPO) phase, and in future AT reactors, depends on the ability to optimize the current profile. While reverse shear increases thermal confinement, the co-alignment of the location of q_{min} and the steep fast-ion pressure gradient drives reversed shear Alfvén eigenmodes (RSAEs), which have been shown previously to cause fast ion transport that degrades core performance in DIII-D [2]. The new experiments have shown that injection of beam power away from the magnetic axis drives off-axis current [1] in agreement with NUBEAM predictions, and it also broadens the
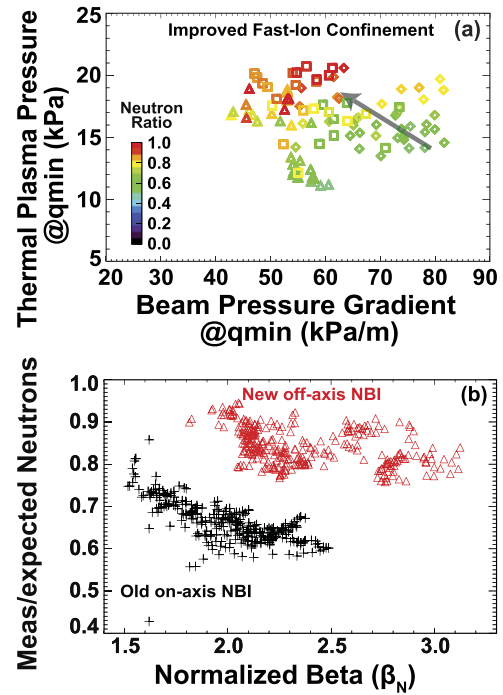

Figure 1. Databases of plasma performance including points with new off-axis NBI. (*a*) Thermal pressure and ratio of measured neutron rate to the rate predicted assuming classical fast ion slowing down (color coding) vs fast ion pressure gradient at the q_{min} location for plasmas with matched total beam power and density using on-axis beams (diamonds), off-axis beams (triangles) and off-axis beams plus on-axis ECCD (squares). (*b*) Ratio of measured to predicted neutron production rate vs core plasma β_ν using only on-axis NBI (black plus symbols) vs with off-axis NBI (red open triangles). Reproduced with permission from [2].

energetic particle (EP) pressure profile [3]. Figure 1(*a*) shows that both the thermal pressure increases and beam pressure gradient decreases using the new increased off-axis neutral beam power. The combination of q_{min} moving to slightly smaller radius and the central fast ion pressure profile broadening, both due to the off-axis NBI, reduces the fast ion pressure gradient in the region of q_{min}. This reduces RSAE drive and increases both core thermal pressure and the maximum achieved ratio of the measured neutron rate to the predicted neutron rate, assuming classical fast ion slowing down (figure 1(*a*)) in scenarios at high toroidal rotation. Fast-ion confinement, indicated by the ratio of measured vs predicted neutrons without AE instability losses, improved by 25% during flattop using the new off-axis NBI (figure 1(*b*)). In the current ramp, further improvements to optimize the q-profile using electron cyclotron current drive (ECCD) resulted in $\sim$36% higher measured neutron ratio than the reference shot. Record parameters of $\beta_N \sim 3.1$ and $H_{89} \sim 2.2$ were achieved for this scenario near the upper end of the DIII-D field capability ($B_T = 2.0$ T) and $q_{95} = 6.0$. These experiments demonstrate an effective fast-ion loss minimization principle that can be used to guide optimization of high-q_{min} operation in ITER and future reactors.

The achievement of more than double the off-axis ECCD efficiency using top launch geometry, compared with conventional low field side (LFS) launch [4, 5], provides a path to substantially increase the off-axis current critical to optimization of the performance and minimization of the cost of future steady state fusion reactors. A prototype top launch system with fixed toroidal and poloidal injection angles utilizing second harmonic X-mode damping was installed on DIII-D to experimentally validate and characterize this approach. Here 'top launch' geometry refers to injection from near the top of the device on the high field side of the magnetic axis, and with a nearly vertical beam trajectory in the poloidal plane projection (figure 2(*a*)). As predicted by CQL3D quasi-linear Fokker–Planck simulations, and verified by experiments which vary the wave-electron interactions in the velocity space by scanning B_T (figure 2(*b*)), the significant enhancement of the ECCD efficiency in the top launch experiments compared with outside launch (figure 2(*c*)) was due to interaction with higher $v_{||}$ electrons that suffer fewer collisions and drive current more efficiently, combined with a longer absorption path for the EC waves to compensate for inherently weaker absorption at higher $v_{||}$. For higher $v_{||}$ interaction (lower B_T) the absorbed EC power was observed to decrease, giving rise to a 'sweet spot' (optimal B_T) for maximum ECCD efficiency (figure 2(*b*)), where the higher current drive efficiency for higher $v_{||}$ is balanced by sufficient absorption. Orienting this sweet spot for absorption vs current drive efficiency at mid-radius, the driven current was 2× higher than for outside launch (figure 2(*c*)). This complete understanding of the mechanisms for enhanced ECCD from top launch geometry can be used to optimize future ECCD systems for power plant scenario needs.

The effectiveness of fast emergency shutdown for disruption prevention during plasma current ramp down after locked mode detection in single-null plasmas at ITER-relevant normalized-currents shows that with optimization at least 50% of ramp down disruptions were delayed until after the plasma current I_p was reduced to ITER-safe normalized-current levels (figure 3(*a*)) [6]. Key to the shutdown result is for the I_p ramp down phase to transition to an inner wall limited (IWL) shape after the locked mode precursor to disruption is detected and emergency ramp down initiated. The overall disruptivity during I_p ramp down was also reduced for IWL ramp downs compared with diverted ramp downs. The applicability of this technique to ITER is under consideration, but the effectiveness achieved points to the importance of early prevention techniques and reliable mitigation tools.

A recently developed algorithm for real-time regulation of proximity-to-instability boundaries has been applied for robust vertical displacement event (VDE) prevention in DIII-D experiments [6]. The algorithm uses either a physics-based or neural-net-based VDE growth-rate estimation to monitor stability, and modifies plasma shaping in real-time to prevent the growth-rate from reaching uncontrollable limits. Figures 3(*b*) and (*c*) show that the controller engages only when it detects that the VDE growth rate has exceeded a pre-programmed
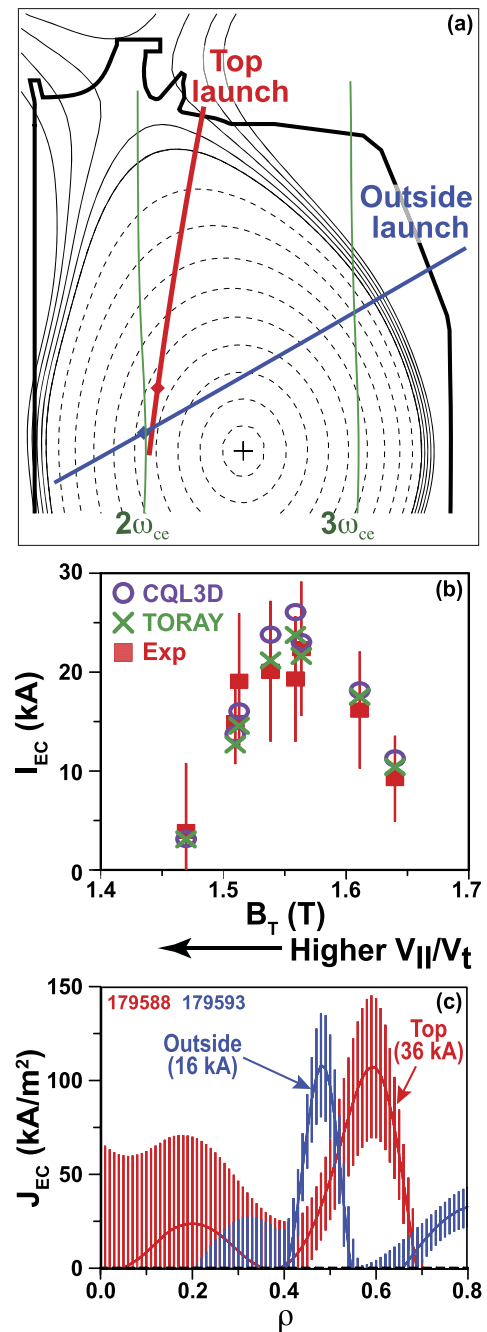

Figure 2. Top launch ECCD results show (*a*) difference in beam path geometry between top (red) and outside (blue) launch, (*b*) optimization of the driven current (red) vs B_T, in agreement with TORAY and CQL3D predictions and (*c*) increased EC driven current density across the profile peaking at mid-radius for top launch (red) compared with outside launch geometry (blue). Reproduced with permission from [5].

threshold value. The VDE is then prevented by real time reduction of the plasma elongation and separatrix to inner wall gap to prevent further increases in the VDE growth rate. Once again, the key for the control is to detect the approach to vertical instability and to modify the plasma shape to maintain stability control. Finally, a novel technique for healing locked mode flux surfaces with 3D fields demonstrated promise for providing current quench (CQ) control by allowing the plasma to
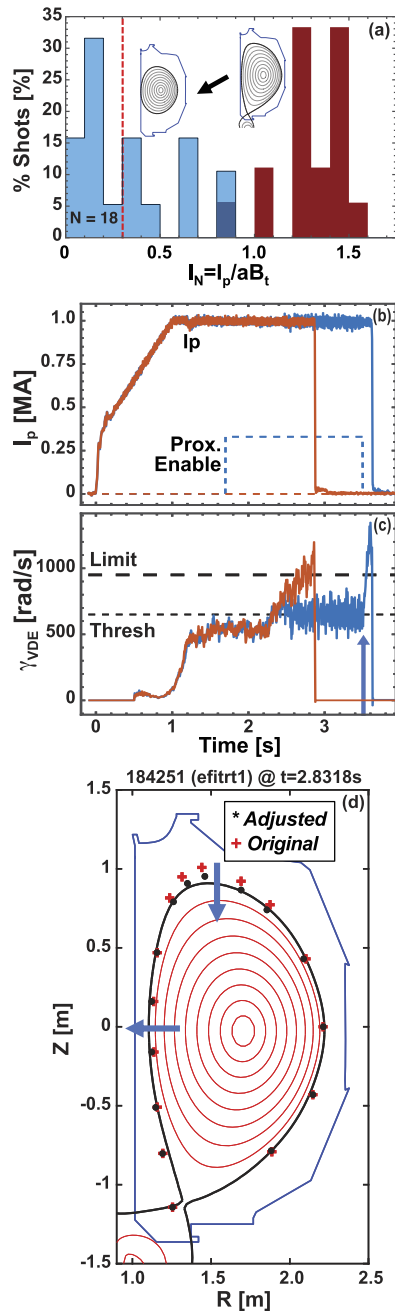
Figure 3. Disruption/VDE avoidance results: (*a*) histogram of emergency shutdown by plasma current ramp down results showing normalized current at flattop (red) and at loss of current (blue) with more than 50% of inner wall limited disruptions below ITER current limits (dashed line). (*b*) Plasma current flattop extended and (*c*) VDE avoided in blue case with controller enabled vs red case without controller, and (*d*) difference of original (red +) and adjusted (black dots) equilibrium control points showing real time control of inner wall gap and plasma elongation for VDE avoidance. Reproduced with permission from [6].

Figure 4. High I_p, low rational q_a RE beam dissipation by kink instability: (*a*) evolution of RE beam current and (*b*) periodic MHD bursts on HFS magnetic probes consistent with. Reproduced from [8]. © IOP Publishing Ltd. All rights reserved. (*c*) MARS-F prediction of final 2/1 external resistive kink, (*d*) resulting increase in RE loss orbits with increased kink HFS amplitude consistent with (*e*) increased spreading of RE hit locations on the first wall (blue +'s) as HFS field perturbation increases, and (*f*), images of IR emission from the center post for RE beam termination without (left) vs with (right) the kink instability. Reproduced courtesy of IAEA. Figure from [9]. Copyright (2021) IAEA.

partially reheat and thereby extend the CQ to a long timescale [7]. In this technique the stochastic field line state at the start of the thermal quench is healed by the applied 3D fields into
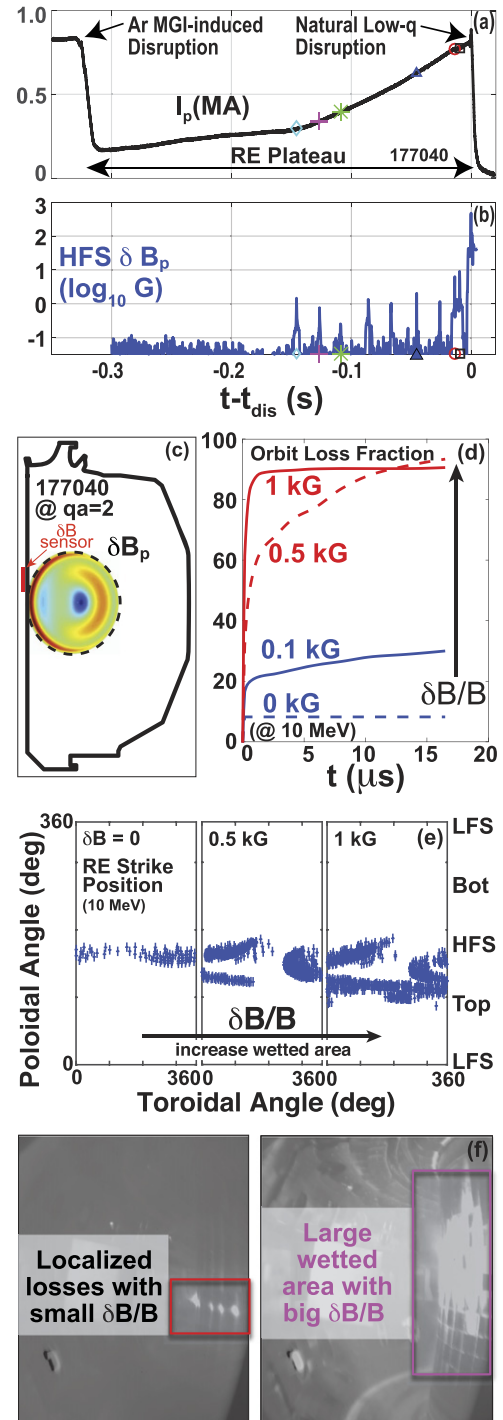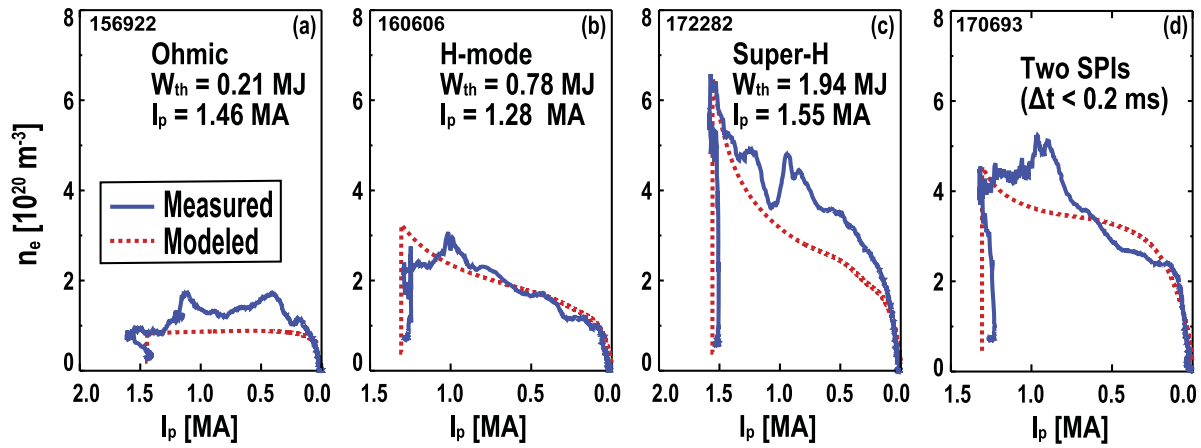
Figure 5. Density evolution during CQ after SPI injection (blue) simulated by energy balance model (red, dashed) for multiple pre-SPI plasma conditions (*a*) ohmic, (*b*) H-mode, (*c*) SH-mode and (*d*) H-mode with dual SPI pellets. Reproduced with permission from [12].

a 3D helical equilibrium with intact flux surfaces, allowing the plasma temperature to partially recover and substantially extending the quench time to final loss of current. This suggests a possible method for a soft-landing of plasma disruptions in the high plasma current regime. Taken together these results show substantial progress toward development of the algorithms and control actuators needed for both disruption/VDE avoidance and mitigation in ITER and future devices.

Studies of high current runaway electron (RE) beams [8, 9] reveal excitation of current-driven (low edge safety factor, q_a) $m/n = 2/1$ kink instabilities (figure 4) that promptly terminate the RE beam on an Alfvenic time-scale, with minimal heating of plasma facing component surfaces [10, 11], offering a new alternate pathway to RE beam mitigation without collisional dissipation. MARS-F modeling [9] predicts that the absence of wall heating is due to both an increase of the wetted area during the MHD-driven RE loss (figures 4(*e*) and (*f*)) and an inhibition of the conversion of magnetic energy into kinetic energy normally observed during RE loss events (when the RE beam regenerates during CQ). Observations of IR emission from the centerpost during RE beam loss (figure 4(*f*)) confirm the MARS-F predictions that the wetted area would include the full toroidal and a substantial poloidal range after the MHD event disperses the RE beam. The experiment also confirms that no RE beam regeneration occurs and instead the original RE current transfers to the cold bulk, which then dissipates the magnetic energy on the timescale of a cold resistive plasma. Variations of D_2 purity by comparisons with experiments using high-Z impurity injection revealed that high D_2 purity was required to obtain recombination of the bulk plasma. This decreased the density and shortened the Alfven time facilitating access to the required low q_a regime and accelerating the large-scale MHD instability terminating the RE beam and preventing the RE regeneration. This result is highly applicable to ITER and future reactors in which the initial RE beam will quickly avalanche to high current and drive edge safety factor low enough to promote

the 2/1 kink instability needed to disperse the RE beam. Initial simulations for ITER scenarios in pure deuterium plasma [10] suggest a multi-step process of RE regeneration, hydrogenic plasma purification and kink mode RE beam dispersal may be required to fully dissipate all remaining RE current, due to the extremely high RE amplification factors anticipated in ITER.

Particle assimilation rates and CQ densities for single and multiple shattered pellet injection (SPI) containing high-Z material (e.g. neon) are shown to be predictable from 0D global energy balance simulations and also from empirical scaling laws, without invoking anomalous MHD mode mixing physics [12]. Straightforward predictions of neon SPI assimilation have been successful by assuming the CQ plasma is radiation limited. The simulations use the 0D KPRAD model [13, 14] with an SPI ablation model that tracks species dependent shielding-limited ablation [15] of the SPI plume, main-ion and impurity ionization, recombination and radiation, ohmic heating and inductive coupling to wall currents. The modeled CQ density evolution agreed well with measurements for neon SPI in DIII-D ohmic, standard H-mode and super H-mode plasmas (figures 5(*a*)–(*c*)). Also, in an H-mode plasma similar to that in figure 5(*b*) before the SPI, the simulated CQ density evolution with two SPI pellets injected within 200 ms of each other was very similar to the measurements (figure 5(*d*)). For deuterium SPI, global energy balance modeling does not match the CQ density evolution and data show that MHD mixing plays a significant role in the CQ timescales [16]. Data and simulations also show toroidal radiation peaking during the thermal quench with single high-Z SPI is close to but not exceeding the factor of 2 surface melt limit [17] set for ITER. Empirical scaling laws for the average CQ density during neon SPI assimilation derived from global parameters like plasma stored energy, and average electron density and temperature are also consistent with global energy balance being the dominant physics. These experiments show that the optimization of global behavior for multiple, high-Z, SPI should now be predictable for ITER and future reactors

3. Fundamental plasma physics understanding and model validation that advance fusion solutions

Plasma rotation scans, and both new non-linear analytic theory [18, 19] and non-linear 2-fluid code simulations [20, 21], confirm that ELM suppression by 3D magnetic perturbations (3DMPs) requires near zero $E \times B$ velocity at the top of the pedestal, and achieving suppression appears to be closely linked to a high field side plasma response. Predictions from substantive recent advances in non-linear theory of 3DMP penetration in rotating plasmas [18, 19] are consistent with non-linear simulations of resonant field penetration using the TM1 [22] and GPEC [23] codes, and results from DIII-D experiments. Using experimental parameters and RMP amplitudes (figure 6(*a*)), TM1 correctly predicts the RMP amplitude required for a bifurcation from screening to penetration of resonant fields at the pedestal top, and also calculates the reduction in the pedestal height and width due to collisional transport across these islands (figure 6(*b*)). The observed density pump-out is reproduced (figure 6(*b*)) from the MHD simulations for the penetration of resonant fields in the resistive foot of the pedestal [20]. From these simulations ELM suppression is seen to correlate with approximately a 15% decrease in the pedestal electron pressure (p_e^{ped}) compared with EPED predictions (figures 6(*a*) and (*b*)). The TM1 simulations also quantitatively explain the required plasma density, rotation and RMP amplitude for the ELM suppression by $n = 2$ RMPs due to the formation of magnetic islands at the top of the pedestal [21]. These MHD simulations reveal strong screening of resonant fields in the steep gradient region between the top and the foot of the pedestal, consistent with the preservation of the edge electron thermal barrier (ETB) during pump-out and ELM suppression.

The long-standing mystery of the q_{95} width of ELM suppression windows has been effectively resolved based on simulations of resonant field penetration at the pedestal top [24, 25]. The TM1 simulations successfully predict that narrow magnetic islands form when resonant field penetration occurs at the top of pedestal, and these islands are easily screened when q_{95} moves off resonance, leading to very narrow windows of ELM suppression (typically $\Delta q_{95} \sim 0.1$ as shown in figures 6(*a*) and (*b*)). For the radial perturbation field used in the experiment (figure 6(*c*) horizontal dashed line), the prediction for the q_{95} ELM suppression windows comes from the windows having at least 15% p_e^{ped} degradation as calculated by TM1 (figure 6(*b*)). TM1 accurately predicts the separated q_{95} windows in which ELM suppression is seen in experiments (width and q_{95} ranges of yellow bands in figures 6(*a*) and (*b*) vs regions with greater than 15% p_e^{ped} reduction at the experimental radial field in figure 6(*c*)) with $n = 3$ structure 3DMPs. TM1 also predicts the observed amount of density pumpout by 3DMPs (figure 6(*b*)). A database of TM1 simulations over a broad operating space in pedestal density and $E \times B$ rotation has been compared with DIII-D ELM suppression results [21] to generate a dimensional scaling relation for the 3DMP penetration threshold. The scaling agrees well with results of full TM1 simulations of ITER cases using predicted baseline
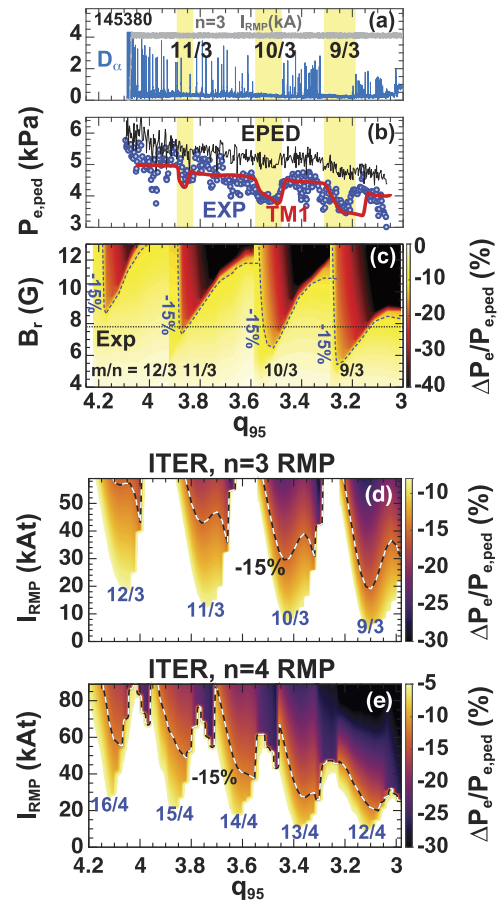

Figure 6. Operational q_{95} windows of ELM suppression: (*a*) $n = 3$ RMP coil current and D_α (upper) showing suppression in the yellow bands, and (*b*) pedestal electron pressure (p_e^{ped}) from experiment (blue), EPED prediction (black) and TM1 prediction (red), (*c*) color contours of TM1 predicted reduction in pedestal pressure versus q_{95} and I_{RMP} for DIII-D and the experimental radial field used (horizontal dashed line), and TM1 p_e^{ped} reduction predictions for ITER with Reprinted figure with permission from [24], Copyright (2020) by the American Physical Society. (*d*) $n = 3$ RMP or(*e*) $n = 4$ RMP. Reproduced courtesy of IAEA. Figure from [25]. Copyright (2021) IAEA.

kinetic and $E \times B$ profiles. The predicted ELM suppression windows (regions with at least 15% p_e^{ped} reduction) for $n = 3$ and $n = 4$ structure 3DMPs (figures 6(*d*) and (*e*)) suggest [25] that ELM suppression should be possible in the ITER $q_{95} \sim 3.1$ range using significantly less than the 90 kAt 3DMP coils currents available in the ITER design. In addition, the $n = 4$ results in particular show that at the 90 kAt limit there may be substantial overlap of q_{95} windows, thereby retaining ELM suppression for a range of plasma currents from about 11–15 MA in ITER [25]. Finally, ELM suppression with 3DMPs is not observed in double-null diverted configurations [26] consistent with theory and code predictions that a high field side response is required for 3DMP field penetration in order to limit pedestal growth that drives the ELM instability. These advances provide the ability to accurately optimize the use of the 3DMP coil set in ITER and future devices for ELM suppression over a wide range of plasma operating parameters, including techniques for minimizing the density pumpout
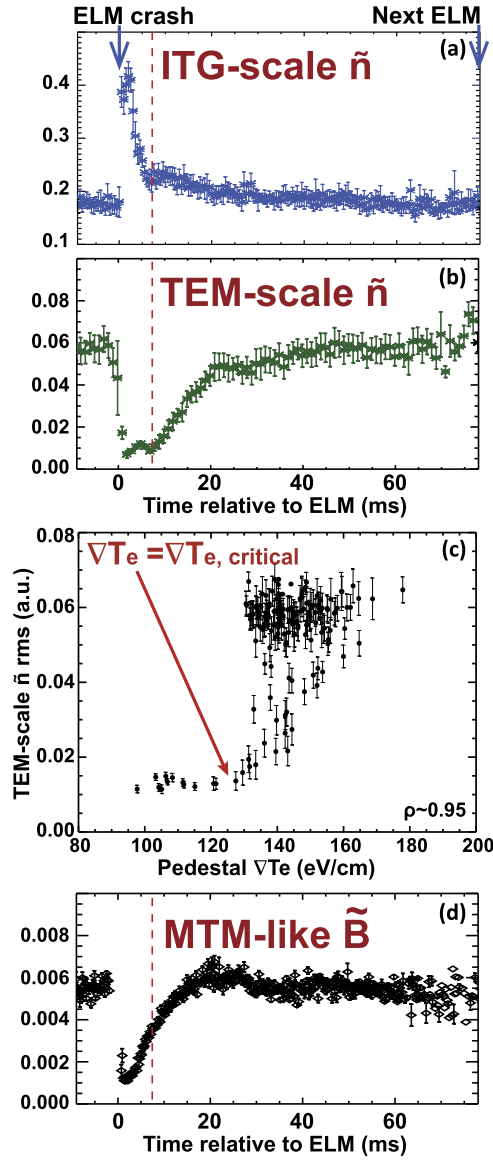
Figure 7. Pedestal fluctuations during the ELM cycle: (*a*) ITG scale modes right after the ELM crash, (*b*) TEM scale modes build between ELMs, (*c*) TEM-scale fluctuations show a temperature gradient threshold and (*d*) MTM scale electro-magnetic fluctuations can also be present between ELMs. Reproduced with permission from [30].

Figure 8. L–H power threshold in hydrogen can be reduced (*a*) by adding small amounts of He for density both at the low (red) and high (blue) range of the broad minimum vs density and (*b*) through NTV torque from 3DMPs, where an estimate of the equivalent expected L-mode torque range in ITER is indicated by the yellow band. Reproduced with permission from [37].

[27] and L–H power threshold increases [28, 29] associated with 3DMP ELM control, and for achieving ELM suppression during variations in plasma current and edge safety factor.

Advances in pedestal physics through new measurements of density and internal magnetic fluctuations, and advances in non-linear simulations, suggest that variations of the electron and ion heat fluxes are consistent with the evolution of multi-scale turbulence in the pedestal. These studies [30–36] identify possible roles for ion temperature gradient (ITG), micro-tearing and trapped electron modes (MTMs and TEMs) in DIII-D pedestal transport. In DIII-D experiments with pedestal ion collisionality $\nu_i^* = 0.9$, observations immediately after the ELM crash show that ITG scale density fluctuations
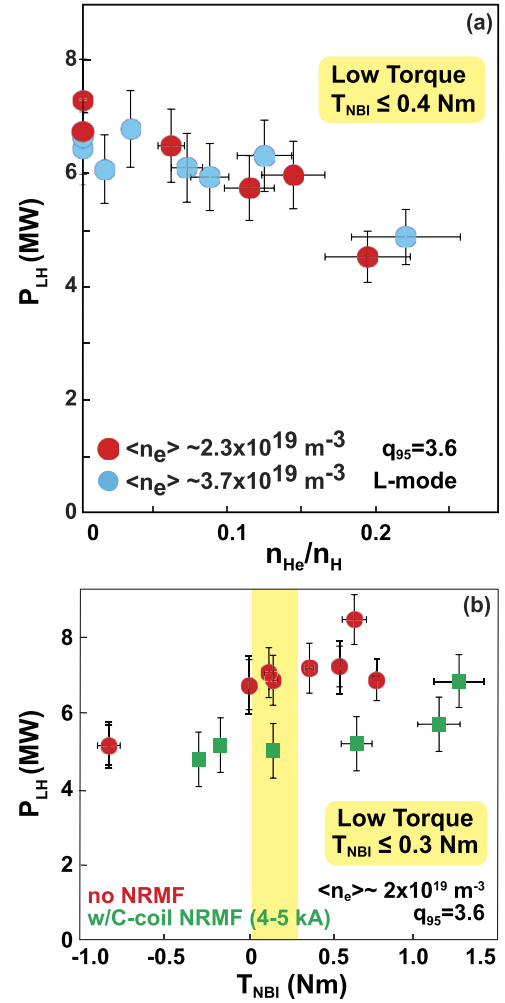
(figure 7(*a*)), predominantly at the bottom of the pedestal, drive ion and electron thermal transport [30]. The density gradient and E_r well reform rapidly and ITG is suppressed by $E \times B$ shear, consistent with the decrease of pedestal ion heat flux (Q_i) from anomalous to near neoclassical. Main ion CER measurements indicate pedestal Q_i becomes increasing anomalous at low collisionality, but at high collisionality Q_i in the pedestal region remains closer to neoclassical [31, 32]. On the longer timescale of the electron temperature gradient (ETG) recovery, the TEM turbulence (figure 7(*b*)) exhibits a threshold in ETG (figure 7(*c*)) and then saturates later in the ELM recovery. MTM scale electro-magnetic modes (figure 7(*d*)) driven by grad-T_e can also contribute to the anomalous Q_e through to the end of the ELM cycle as suggested by non-linear simulations [32–34], although their experimental identification is not yet conclusive in this set of experiments. Finally, simulations predict that ETG modes also contribute to Q_e between ELMs [36], although the spatial scales are so short that no direct measurements of ETG scale fluctuations in the pedestal are
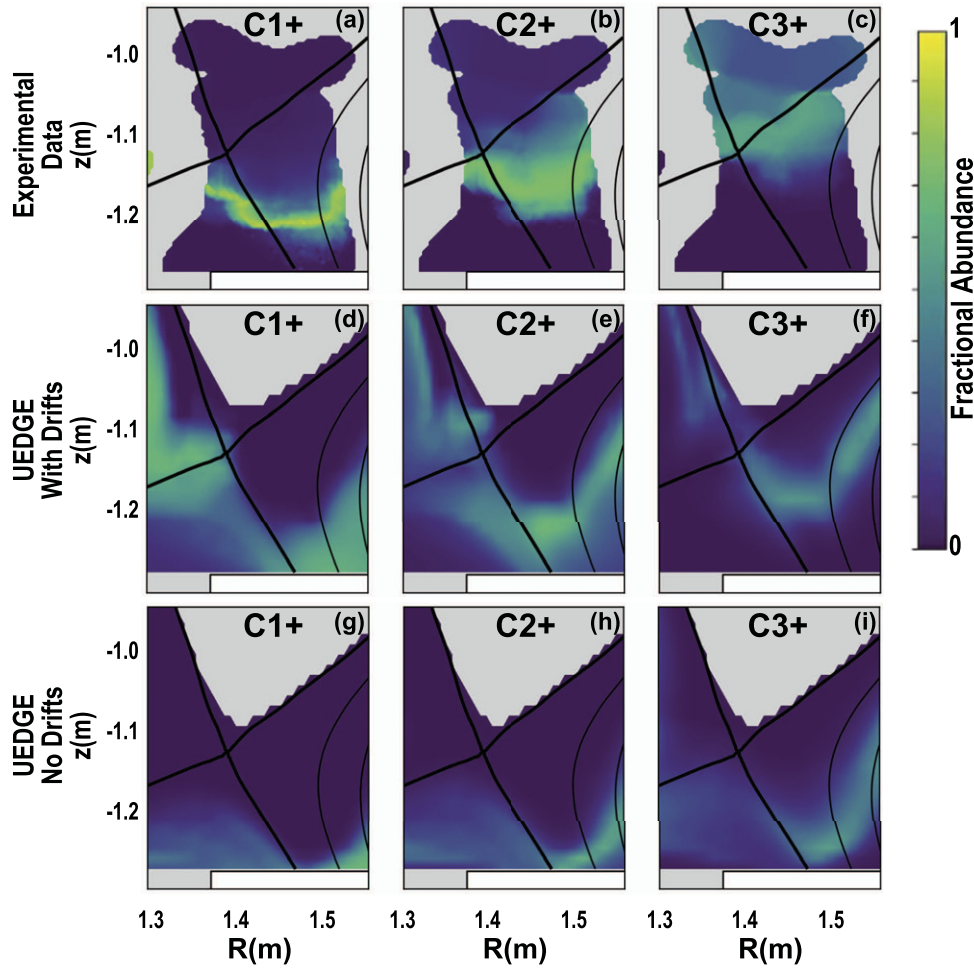
Figure 9. Carbon impurity distributions: color contours of (*a*) several charge state fractional abundances calculated directly from measured divertor n_e, T_e and EUV/VUV resonant line emissivity, (*b*) predicted fractional abundances from UEDGE simulations with full poloidal and radial drifts and (*c*) predictions without drifts. Reproduced with permission from [38].

available. This detailed understanding of the turbulent thermal transport drives in the pedestal significantly improves our ability to understand inter-ELM pedestal transport for projections to ITER and future devices.

To contribute to the ITER research plan urgent tasks, recent experiments with hydrogen plasmas in DIII-D at low input torque, similar to the first ITER non-nuclear pre fusion power operation (PFPO-1) phase, show that the L–H power threshold was reduced [28, 29, 37] with either small admixtures of helium or by using non-resonant 3DMP fields to produce edge counter-current neoclassical toroidal viscosity (NTV) torque (figure 8). Low rotation H-mode operation of hydrogen plasma was achieved in these experiments with a combination of toroidally balanced hydrogen NBI and ECH power. P_{L-H} was reduced about 30% (figure 8(*a*)) by adding <=20% helium ions to the hydrogen plasma for densities spanning the broad minimum in P_{L-H}. The P_{L-H} threshold in hydrogen plasma without helium seeding was also reduced 20%–30% (figure 8(*b*)) at ITER relevant input torque using $n = 3$ non-resonant 3D perturbation fields from the DIII-D external coils at 3DMP levels consistent with the capabilities of the ITER internal coils. These experiments identify two actuators that could be used to reduce the L–H power threshold in the non-nuclear phase of ITER, where H-mode access is likely

challenging in particular at high fractions of the Greenwald density.

The ability to predict the impurity seeding needed for divertor dissipation has advanced through the new capability for measuring charge-state resolved densities of impurity species in the divertor [38] and validation of SOL and divertor fluid modeling with full poloidal and radial drifts. By combining EUV/VUV measurements of resonance emission lines [39] with local electron density and temperature measurements from Thomson scattering and a collisional radiative model framework, the 2D density distributions of all the charge states of carbon (examples in figure 9(*a*)) were calculated for the DIII-D divertor plasma in both attached and detached H-mode conditions. UEDGE simulated profiles (figures 9(*b*) and (*c*)) were quantitatively much closer to the measured 2D distributions when full poloidal and radial drifts were included in the modeling (figure 9(*b*)) than for corresponding simulations without the drifts (figure 9(*c*)). Note that for the example plasma shown, the experimental data indicates the outer divertor is detached, which is consistent with the fractional abundances of C^{1+}, C^{2+} and C^{3+} all being peaked progressively farther off the target plate poloidally as charge state increases. The simulation with drifts reproduces these characteristics of

the charge state distributions in detachment, but the case without drifts shows a qualitatively incorrect fully attached outer leg with these charge states peaking very near the target surface. This qualitative difference in the simulations emphasizes the importance of including the full radial and poloidal drifts in the calculations. The data showed that fractional abundance of the various charge states within the total carbon density had a strong spatial variation, as did the total carbon density normalized to the electron density. These fractional abundances were also strong functions of the divertor conditions; the measured carbon fraction of the electron density decreased by $10\times$ from attached to detached conditions, with similar but slightly smaller reduction factors in the comparison of simulations with full drift effects. The carbon fraction needed for strike point detachment estimated from simplified 1D SOL models (e.g., [40–42]) was about a factor of 2 higher than inferred from these detailed 2D data. These data will validate and improve aspects of the fluid code modeling with full drifts, and the validated codes are directly applicable to ITER relevant scenarios in which other impurity species (e.g., nitrogen or neon) are proposed to be used for divertor detachment control.

With these advances, experimental data using impurity injection and SOLPS-ITER simulations with full drift effects show that for the small angle slot (SAS) baffling geometry in the upper divertor of DIII-D, divertor detachment and pedestal performance can be optimized through magnetic geometry and choice of impurity species [43, 44]. Experiments with nitrogen injection show that a larger quantity of impurity is required to detach the SAS divertor plasma (figure 10(*a*)), and a higher density of nitrogen appears in the pedestal and core plasma (figure 10(*b*)) when the outer strike point (OSP) is in the outer corner of the slot (red) compared with the OSP positioned on the inner slanted surface of the SAS (blue) [43, 44]. SOLPS-ITER modeling with full cross-field drifts and both carbon and nitrogen impurity charge states is required to reproduce these effects. The modeling shows that the differences are due to changes in the stagnation point location of the main ion cross field flow profiles and changes in the entrainment of nitrogen ions in those flows as a result of the geometry change [44]. Experiments using the optimum magnetic geometry with the OSP on the inner slanted baffle in the SAS found that the choice of impurity species (neon vs nitrogen) injected into the SAS outer leg had little effect on the upstream pedestal T_e profiles (figure 10(*d*)), but the pedestal density gradient was significantly higher and separatrix density significantly lower with neon injection (figure 10(*c*)). These experiments, and the comparison to modeling with full drifts and impurity charge states, increase confidence in predictions of divertor detachment optimization by choice of strike point geometry and impurity species.

Simulations of the radial migration of tungsten from a nearly toroidally continuous ring embedded in the carbon divertor tiles (figure 11(*b*)) reproduce the observed redeposition of a W:C layer outboard of the source ring only when $E \times B$ drift effects are taken into account (figure 11(*a*)) [45, 46]. These simulations and measurements were taken from the DIII-D campaign of lower single null (LSN) plasmas with
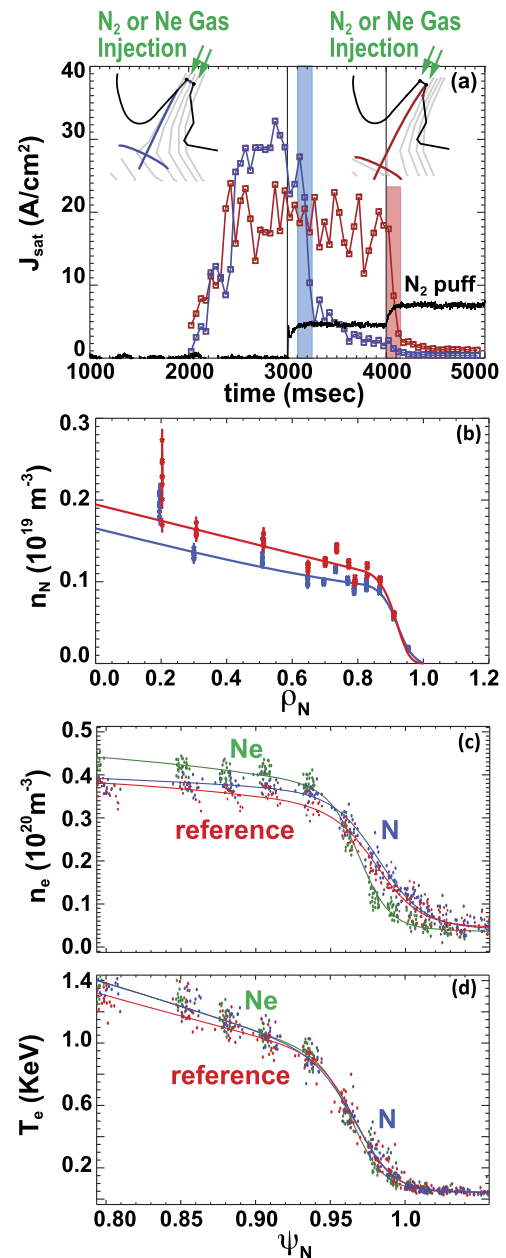

Figure 10. SAS impurity injection: (*a*) dependence of outer strike point (OSP) ion saturation current (J_{sat}) at detachment (vertical shaded bands) as a result of nitrogen injection (black curve) for different geometry of the OSP location in a closed SAS divertor-inner slanted baffle (blue) vs outer slot corner (red). Insets show the geometry of the OSP and the locations of gas injection (*b*) profiles of core nitrogen density at the same electron density (colors correspond to the OSP geometry in (*a*)), Reproduced with permission from [44]. (*c*) pedestal electron density and (*d*) electron temperature profiles with the OSP on the inner slanted baffle comparing a reference case without impurity injection (red), a case with nitrogen injection (blue) and a case with neon injection (green). Reproduced with permission from [43].

the tungsten ring in the lower divertor [47]. Mixed material DIVIMP-WallDYN modeling [45] including $E \times B$ drifts is more consistent with the observed redeposition profile (diamonds in figure 11(*a*)) than modeling that neglects $E \times B$ drifts; however, simulations using 60% of the theoretical drifts
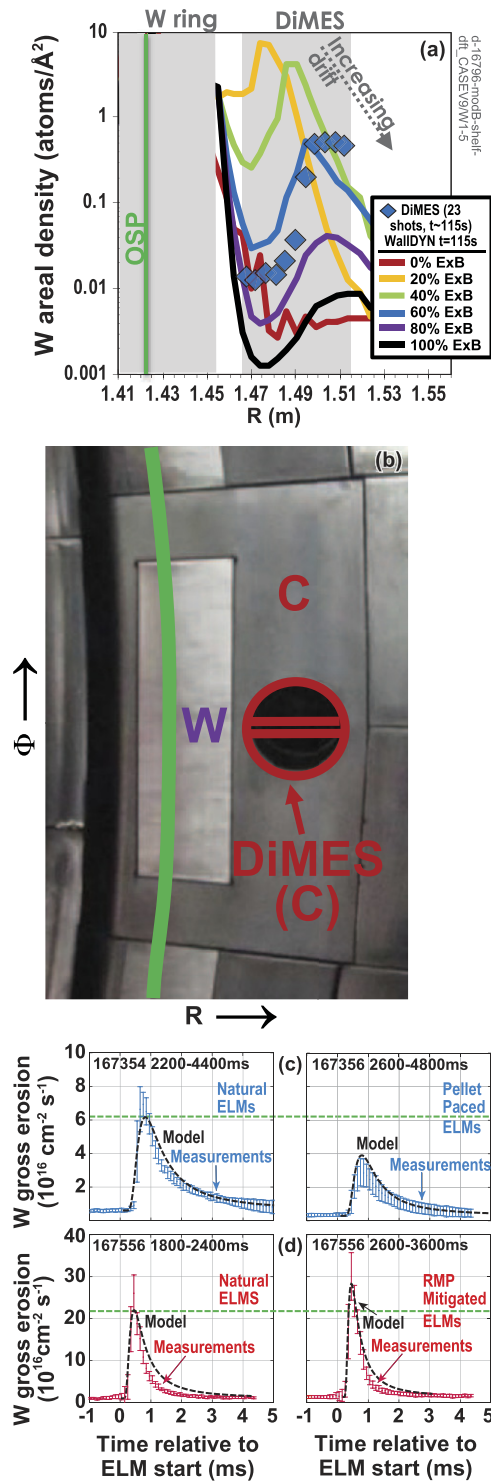
Figure 11. Tungsten erosion and migration: (*a*) measured tungsten radially outward redeposition (diamonds) on DiMES removable sample probe from a toroidal tungsten ring geometry ((*b*)—vertical view)) compared with simulations using fractions of the theoretical $E \times B$ drift effects (curves and legend), and Reproduced courtesy of IAEA. Figure from [45]. Copyright (2021) IAEA. (*c*) and (*d*) intra ELM W gross erosion for (*c*) natural ELMs (left) vs ELMs mitigated by pellet pacing (right) and for (*d*) natural ELMs (left) vs ELMs mitigated by RMP fields (right). In all cases the evolution of the gross erosion matched by FSRM prediction (dashed black). Reprinted from [48], with the permission of AIP Publishing.

for the attached L-mode conditions of the experiment turn out to be more consistent with measurements than predictions assuming the full theoretical magnitude of the drifts. This result suggests that additional physics such as the effect of SOL currents on the calculated radial electric field need to be taken into account in the magnitude of the $E \times B$ drifts. This work identifies the important physics controlling the radial migration both in terms of the mixed material environment relevant to the W, Be situation in ITER and the importance of the poloidal particle drifts, which will be very strong in many phases of ITER operation.

Modeling of intra-ELM tungsten gross erosion from the continuous toroidal ring [47] with an analytic free-streaming plus recycling model (FSRM) [48, 49] is now validated in ITER-relevant mitigated-ELM regimes using pellet pacing and RMPs (figures 11(*c*) and (*d*)) [49]. For pellet paced ELMs the FSRM reproduces the observation that the peak intra-ELM W gross erosion is reduced compared with natural ELMs (figure 11(*c*)). In this case the pedestal n_e and T_e remained nearly constant but the ELM frequency was increased $2\times$ by the pellets and, as a consequence, the pedestal carbon content was decreased almost a factor of 2. Since intra-ELM W sputtering is strongly affected by C^{6+} ions, the reduction in pedestal carbon content contributed to the reduction in W erosion, as reproduced by the FSRM. For ELM size mitigated but not completely suppressed by 3D magnetic fields (figure 11(*d*)), the FSRM again reproduces the observation that the peak intra-ELM W gross erosion increases slightly compared with natural ELMs. In this case the effect of the 3D fields was to reduce the upstream pedestal density at nearly constant pedestal temperature, and thereby produce a strong reduction in the divertor target density and a 20% increase in target T_e. By taking the effects of these changes in target plasma conditions properly into account, the FSRM again reproduced the intra-ELM W sputtering evolution. These experiments, with a radially localized source of tungsten, help to validate erosion and redeposition models to increase predictability of tungsten behavior in ITER.

4. Scenarios integrating high performance core and boundary

Integration of a high-performance core plasma and a low temperature solution for the plasma at the divertor targets has been demonstrated in a high poloidal beta scenario that features large Shafranov shift, internal transport barriers (ITBs) in n_e, T_e and T_i coupled to a detached divertor using active feedback-controlled N_2 or Ne puffing [50–54]. Theory-based modeling suggests that similar plasmas in ITER FPO phase with planned heating systems could be consistent with $Q = 10$ at reduced plasma current of 7–9 MA [51]. In the DIII-D experiments, feedback control of either nitrogen or neon was used to control the degree of detachment of the divertor while coupling to a high-performance core plasma at high poloidal beta (nitrogen case shown in figure 12) [50, 52, 53]. This example shows the characteristics of the core–edge coupling achieved with either nitrogen or neon impurity seeding. With
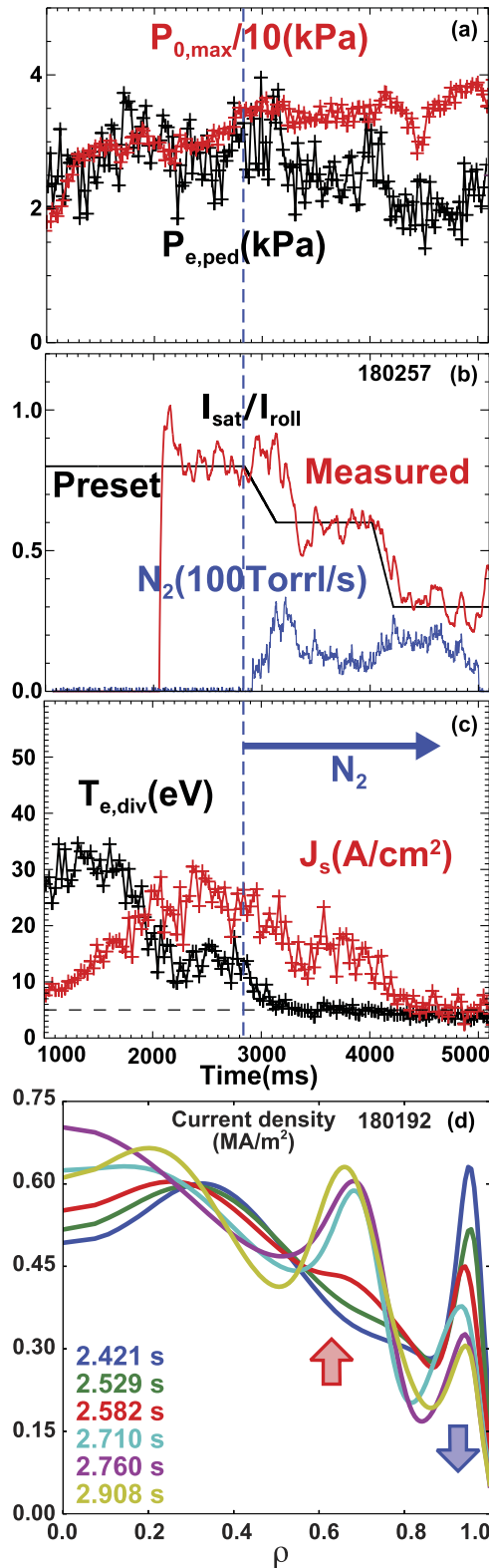
Figure 12. High β_p scenario: with nitrogen injection (dashed line) (*a*) pedestal pressure (black) and central pressure (red), (*b*) nitrogen gas rate (blue) and I_{sat}/I_{roll} ratio (red) vs target values (black), (*c*) target ion saturation current (red) and target T_e (black) and Reproduced from [52]. CC BY 4.0. (*d*) reconstructions of core current density profiles from times before to after ITB formation. Reproduced with permission from [51].

sufficient impurity injection (figure 12(*b*)) the ion saturation current at the divertor outer strike point achieves roll over and the electron temperature measured with probes drops below 5 eV across the entire divertor plate (figure 12(*c*)). At the same time pedestal pressure is also reduced due to impurity radiation but high central core pressure is retained (figure 12(*a*)). Injection of the impurity in the divertor helped to trigger the formation of an internal transport barrier at large radius in the core density, and both electron and ion temperature profiles, compensating for the reduction in pedestal pressure and enhancing the performance parameters to $H_{98y2} = 1.5$, $\beta_N = 3$, $\beta_p > 2$, at $q_{95} = 7.8$. In separate high β_p experiments, large radius ITBs were also obtained with strong deuterium gas injection [52, 53]. The high β_p configuration lends itself to ITB formation due to a combination of Shafranov shift stabilization of turbulence, high bootstrap current generation at high q_{95} and high q_{min} at large radius [54]. Impurity injection and radiation at the plasma edge enhances the redistribution of bootstrap current from near the very edge to a large radius ($\rho = 0.7$–0.8) location in the core as the pedestal pressure and its gradient are reduced (figure 12(*d*)). This current redistribution decreases the local magnetic shear at this location allowing the plasma to self-organize to a stable low transport state with high local pressure gradients (the ITB). The experiments with neon injection also demonstrated suppression of ELMs during the coupling of high core performance and a detached divertor [52]. Based on these results, self-consistent equilibrium and 1D transport modeling of an ITER scenario, using the TGLF code with the same turbulence saturation rule that matches the measured profiles in simulations of the DIII-D discharges, shows that the $Q = 10$ goal for ITER is predicted at $I_p = 7$–9 MA, $\beta_N = 2.8$ and $P_{fus} = 300$ MW using the ITER day-one heating systems [51]. This represents a possible alternate scenario to achieve the $Q = 10$ ITER mission at lower risk to the device from disruptions and type-I ELMs due to the reduced plasma current. The high β_p scenario at this reduced current is also predicted to achieve ITER's 500 MW fusion power goal at $Q \sim 40$, albeit with higher $\beta_N \sim 3.2$. The DIII-D experiments validate the simulation predictions of ITB formation and high performance in an ITER high β_p scenario at reduced plasma current.

High density and stored energy plasmas with super H-mode (SH) edge pedestals [55, 56] were made both in a lower single null (LSN) shape accessible by JET [57] and in a higher triangularity near double null shape coupled at least transiently to a radiative divertor [58] for target heat flux control using nitrogen injection for substantial ($\sim$80%) radiated power fraction in a core–edge integrated scenario (figure 13). Super H-mode pedestal operation has also been obtained in an upper single null (USN) shape with a more closed divertor baffling configuration. Prior to the LSN experiment, calculations with EPED [59] predicted that enhanced pedestal pressure in the SH channel would be accessible in an LSN plasma with moderate shaping accessible in JET. Stationary operating points at peeling-limited pedestal pressures far up the SH channel were achieved (figure 13(*a*)), although at lower absolute pressures
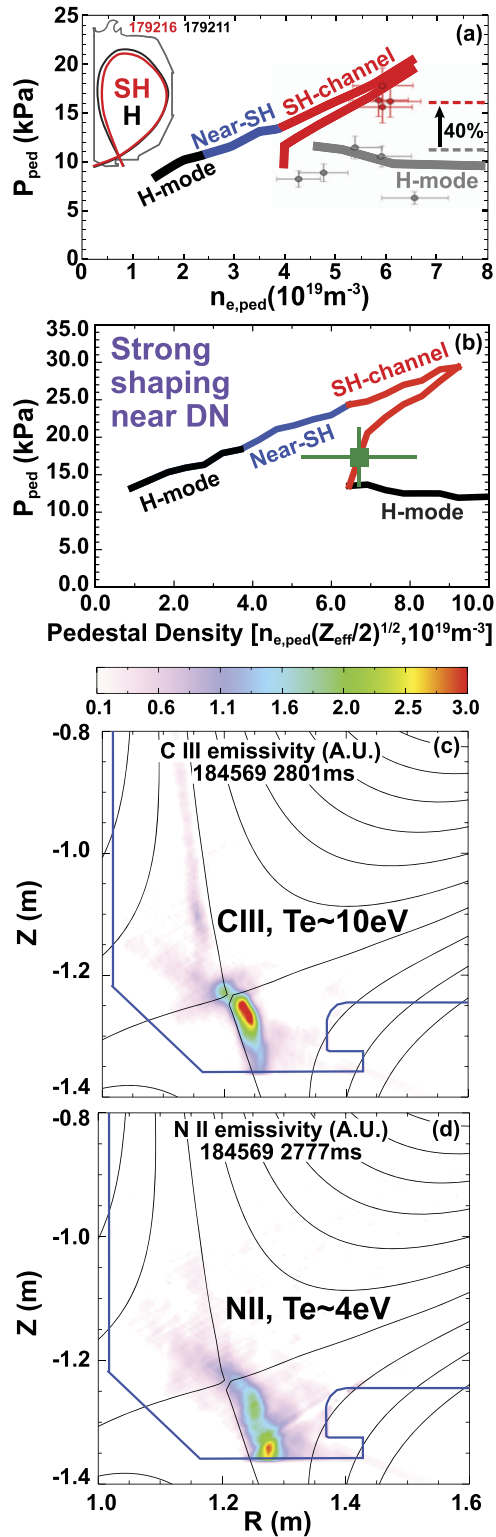
Figure 13. Super H-mode pedestal operation: (*a*) operation far into SH-channel in pedestal density vs pressure space (red points) vs standard H-mode (gray) in an LSN shape compatible with JET operation, and (*b*)–(*d*) for a more highly shaped near DN plasma several energy confinement time operation Reprinted from [57], with the permission of AIP Publishing. (*b*) at the entrance to the SH-channel (green point) with (*c*) C^{2+} radiation indicative of $T_e \sim 10$ eV near the X-point and (*d*) N^{1+} emission ($T_e \sim 4$ eV) near the target plate. Reproduced with permission from [58].

than obtained transiently for SH operation in highly shaped double null (DN) plasmas [58]. The pedestal pressure in these high-density plasmas was about 40% higher than comparable plasmas in the same LSN shape operating with a ballooning limited pedestal at similar densities (figure 13(*a*)). Building on these results, EPED analysis of ITER LSN scenarios showed potential for operation in the SH-mode channel with up to a 50% enhancement of the pedestal pressure compared with H-mode [57, 60].

In the SH-mode experiments with highly shaped DN plasmas [58], simultaneous pedestal operation for several energy confinement times at the entrance to the SH-mode channel and radiative divertor operation with divertor strike points at the onset of detachment was obtained using nitrogen injection (figures 13(*b*)–(*d*)). In these cases the pedestal pressure remained on the second stability solution at the entrance to the SH channel (figure 13(*b*)), and higher than for standard H-mode in the same shape, for several energy confinement times after impurity injection [57, 58]. Total radiated power fraction in these discharges was up to 80% of the input power dominantly in the lower divertor and exceeding the 70% radiated power fraction target for ITER scenarios. Divertor line radiation (figures 13(*c*) and (*d*)) confirmed that T_e near the outer strike point was reduced to ~ 4 eV (figure 13(*d*)) and T_e in the SOL near the X-point was reduced to ~ 10 eV (figure 13(*c*)). In addition, target T_e and ion saturation current ($J_{\rm sat}$) from floor probes, and the observed 30% reduction of the measured outer divertor strike point (OSP) heat flux, confirmed the OSP was at the onset of detachment during the time the high pedestal pressure was maintained [58]. Advanced control algorithms [61, 62] were used to achieve these results including the use of feedback-controlled 3D fields for density control and feedback nitrogen gas puffing for divertor radiated power control. All of these results suggest that it may be desirable to look into SH-like pedestal pressure enhancements in ITER scenarios with detached radiative divertors.

TRANSP simulations confirm that a high-performance hybrid core scenario, experimentally maintained with $q_0 > 1$ (figure 14) and no sawteeth using off-axis ECCD, could be explained directly from the calculated off-axis driven current without invoking anomalous current diffusion physics [63]. In previous TRANSP simulations of hybrid core operation with on-axis ECCD (figure 14(*a*)), the simulated evolution of central safety factor, q_0, without invoking anomalous current diffusion physics did not match the measurement. Simulations of the experiments with off-axis ECCD matched the evolution of q_0 well using only the calculated profiles of the driven current (figure 14(*b*)). Similar performance of the steady state hybrid regime with on-axis ECCD was also achieved using off-axis ECCD aimed at $\rho = 0.45$ (figure 14(*c*)), with no sawteeth for greater than 1.5 current diffusion times, $\beta_N = 3.7$, $H_{98y2} = 1.6$ and $q_{95} = 6$. These high beta, high density hybrid scenarios in DIII-D project with ρ^* scaling to $Q = 5$ in ITER at $I_p = 8.3$ MA and pedestal Greenwald fraction of 0.9. Also high-performance hybrids were demonstrated to be compatible with radiative divertor operation using neon or argon
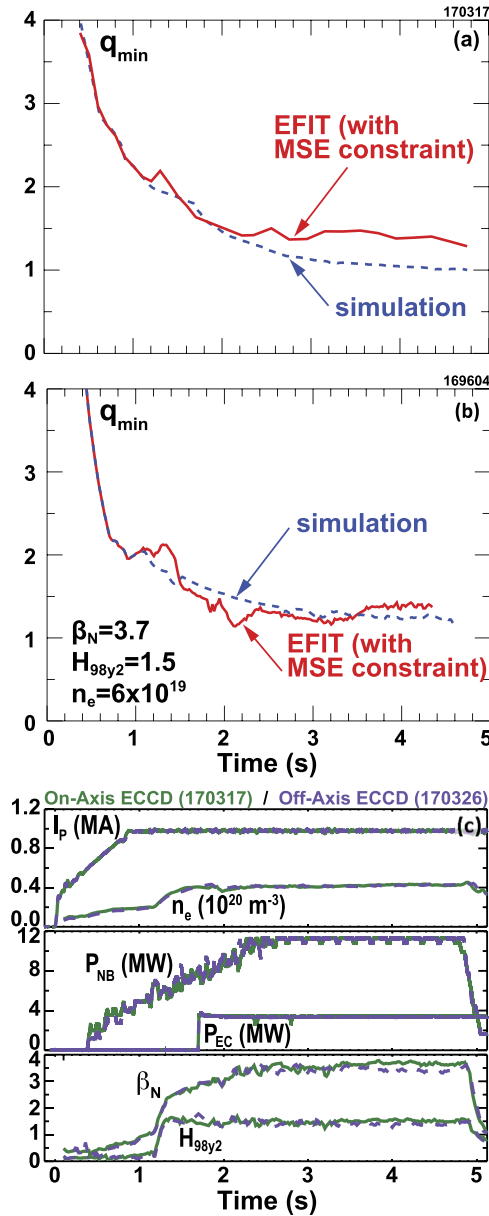
Figure 14. Hybrid scenario: (*a*) measured q_{min} evolution (red) in hybrid plasmas with on axis ECCD vs TRANSP simulations without anomalous current diffusion (blue), (*b*) TRANSP simulations without anomalous current diffusion (blue) vs the q_0 evolution using off-axis ECCD (red) and (*c*) time evolution of the current, density, NBI and EC power, β_N and H_{98y2} for on-axis (green) vs off-axis (purple) ECCD. Reproduced with permission from [63].

Figure 15. Negative triangularity shape: (*a*) database of high, β_N and $H_{98,y2}$ performance of inner wall limited negative triangularity (NegD) plasmas (blue) and a diverted configuration with an L-mode edge and negative average triangularity (red) and (*b*) broader SOL heat flux profiles (both normalized to the peak value) from the diverted NegD plasmas with the L-mode edge vs an H-mode edge case at less pronounced NegD. Reproduced courtesy of IAEA. Figure from [68]. Copyright (2021) IAEA.

gas injection [64]. Core impurity peaking in these hybrids was substantially reduced using near-axis ECH heating. This new demonstration of control of current profile broadening in hybrid core plasmas increases confidence in steady state $Q > 5$ ITER hybrid scenarios with off-axis current drive.

Experiments in the ITER baseline scenario showed that the plasma magnetic response to oscillating probing fields provided a sensor for assessing proximity to stability limits and regulating β_N [65]. MARS-F simulations of resistive MHD, with plasma rotation included, reproduced the dependence of the plasma response to sinusoidal probing fields of various frequencies with variation of rotation, li and β_N. Using
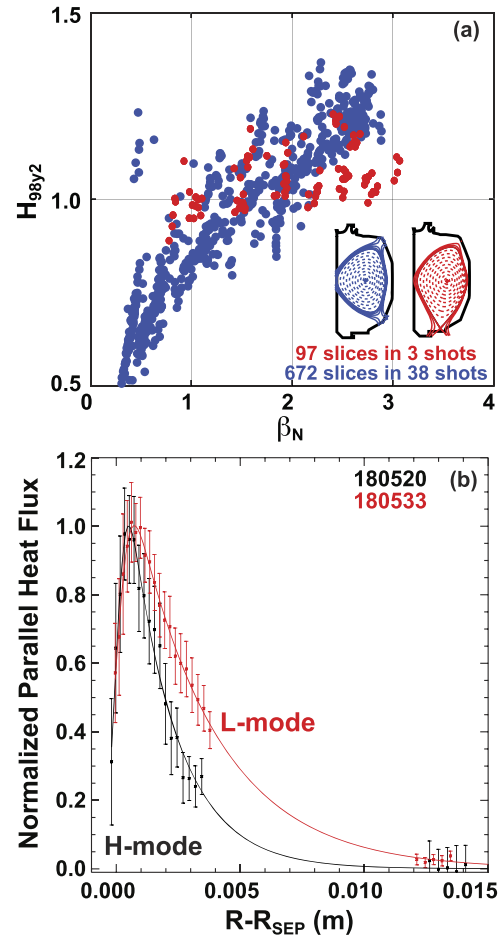
active magnetic spectroscopy (AMS) frequency and amplitude scans, a controller was optimized and demonstrated that the plasma response could be kept away from levels correlated with mode locking by feedback on the injected NB power [65]. This suggests that AMS could be an attractive technique, applicable to ITER and future devices, for avoiding stability limits.

Finally, plasma scenarios with an innovative negative triangularity shape were obtained with high confinement factor, significant normalized beta and an L-mode like edge without ELMs [66–69]. A database of timeslices for both inner wall limited and LSN diverted negative triangularity plasmas (figure 15(*a*)) shows confinement factors H_{98y2} up to 1.4 and β_N up to 3.0. Detailed TRANSP analysis of the highest performing of these plasmas is underway, with indications the confinement enhancement may be slightly lower (H_{98y2} up to 1.2). High power injection into an LSN diverted shape with large average negative triangularity maintained an L-mode edge without ELMs up to 5× the L–H power threshold scaling for positive triangularity. Stability analysis for the edge of

these plasmas showed that ballooning modes closed off the access to second stability and prevented growth of the pedestal to the ELM instability boundary [69]. The scaling of the total stored energy with injected power in these plasmas was significantly stronger than that predicted by the ITER-89P scaling law, which was derived for positive or near-zero triangularity. Plasmas with marginally less negative average triangularity developed an H-mode edge and ELMs at the normal L–H threshold power, suggesting a threshold in the degree of negative triangularity needed to retain the L-mode edge [68]. The SOL width in the L-mode edge cases without ELMs was up to 50% broader than the inter-ELM SOL width for the H-mode case at slightly less negative triangularity (figure 15(*b*)). Normalized impurity particle confinement in the strongly negative triangularity diverted shapes was low ($\tau_{imp}/\tau_E \sim 1$) consistent with the L-mode edge, no central impurity accumulation and $Z_{eff} \sim 1.5$. These initial observations are all attractive features of the negative triangularity plasma shape for projections toward future fusion pilot plants.

5. Summary and future plans

The DIII-D physics program is addressing critical challenges for the operation of ITER and the next generation of fusion energy devices through a focus on innovative solutions for high performance steady state operation, coupled with fundamental plasma physics understanding and model validation, which drives the development of scenarios that integrate high performance core and boundary plasmas. Recent experiments have combined new injected power systems and increased understanding of physics mechanisms, to optimize several candidate core–edge integrated scenarios for future fusion pilot plants.

Progress has been made toward the goals of validated heating and current drive models applicable to ITER and current profile control techniques for optimization of future steady state tokamak reactors [70]. Use of an additional off-axis neutral beam injector from a recently upgraded 5 MW co-/counter-I_p steerable beamline reduced the fast ion losses due to AE instabilities and improved the performance of AT high q_{min} scenarios. Vertical top launch of EC power increased the ECCD efficiency by a factor of 2 for off-axis deposition. Calculations indicate that planned high harmonic fast wave (HHFW) injection [70–73] with a recently installed helicon antenna, and planned unique high field side (HFS) lower hybrid (LH) slow wave injection [70, 74] will contribute substantially to the ability to control the current profile in the high-density core plasmas [75] needed to couple to effective radiative divertor solutions in DIII-D.

Significant progress has been made to address critical issues for ITER operation including in the areas of disruption prediction, avoidance and mitigation, runaway electron beam dissipation, ELM control, H-mode operation in the nonnuclear phase, and material migration from target erosion. New machine learning based proximity-to-instability algorithms connected to plasma shape actuators were effective

to avoid VDEs. After detection of pending disruption, inner-wall-limited techniques for emergency plasma shutdown were effective to ramp down I_p below the required ITER limits before any disruption. Experiments find that at high RE current density (low rational edge safety factor) and in the presence of deuterium injection, a large external kink instability terminates the entire high energy runaway population and disperses it over a large area of the wall, while also avoiding RE regeneration. Non-linear simulations can now predict the isolated q_{95} windows where ELM suppression is expected to occur from the application of 3D magnetic perturbation fields. Two different techniques within ITER's capabilities were shown to significantly lower the L–H power threshold for dominantly hydrogen plasmas characteristic of the planned ITER non-nuclear phases. Direct measurement of impurity charge state distributions for both attached and detached divertor operation now challenge and validate 2D SOL and divertor plasma models, identifying the critical role of poloidal and radial cross field drifts. Results from impurity injection into the SAS divertor also challenge and validate the SOL and divertor fluid codes with full drift effects. Finally experiments showed that explaining observed tungsten migration required taking into account effects due to $E \times B$ drifts, and tungsten erosion during ELMs mitigated by several techniques had a strong dependence on the effect of the technique on the plasma conditions near the target surface.

Recent developments in integrating high performance core and edge solutions showed promise in plasmas with high poloidal beta and an internal transport barrier, plasmas with an enhanced Super H-mode pedestal pressure, plasmas with a hybrid core having central $q_0 > 1$, and plasmas with a high negative triangularity shape. Plasmas with a high β_p and an ITB facilitated by divertor impurity injection (nitrogen or neon) showed excellent core performance parameters simultaneously with detached low heat and particle flux divertor target plasma. Highly shaped plasmas with elevated SH-mode pedestal pressure were coupled to a radiative divertor at the onset of strike point detachment using nitrogen injection. Experiments also demonstrated access to enhance SH-mode pedestal pressure in moderately shaped LSN plasmas accessible in JET and ITER. Plasmas with increased off-axis current drive sustained hybrid core operation at high β_N without sawteeth for multiple current diffusion times, and simulations showed that central q_0 remained above 1.0 without invoking anomalous current diffusion physics. Finally, innovative plasmas with a strongly negative triangularity shape operated at good H-mode-like confinement and core β_N but with an L-mode-like edge, broad SOL heat flux width and no ELMs. Each of these scenarios displays many of the features needed to optimize tokamak operation in reactor relevant regimes.

In 2021 and beyond the DIII-D program will install additional tools for optimizing tokamak operation through core plasma current and heating profile control, and will continue work to couple high performance core operation to edge plasma solutions for steady state and transient heat and particle fluxes [70]. Core optimization through current and pressure

profile control will be investigated using a 1 MW LFS helicon HHFW CD system [76], a unique HFS lower hybrid CD system [77], and increased ECH power including additional top launch injectors. Edge plasma and plasma materials interactions solutions will be explored using a new high power closed divertor geometry [78] and a wall insertion test station for macroscopic scale innovative materials testing. For the longer term, major upgrades to both the normalized and absolute capabilities of the facility are being considered to increase performance and flexibility in order to resolve the physics and techniques for integrated core–edge solutions in the relevant physics regimes for future fusion reactors. Additional issues critical to optimization of power plant performance would be addressed for example with proposed installation of a new high toroidal mode number array of internal midplane 3DMP coils [79] and a passive RE mitigation coil [80]. These and many other tools will enhance the ability of the DIII-D facility to address the important issues needed to provide the physics basis for optimizing the tokamak approach to fusion energy production.

Disclaimer

This report was prepared as an account of work sponsored by an agency of the United States Government. Neither the United States Government nor any agency thereof, nor any of their employees, makes any warranty, express or implied, or assumes any legal liability or responsibility for the accuracy, completeness, or usefulness of any information, apparatus, product, or process disclosed, or represents that its use would not infringe privately owned rights. Reference herein to any specific commercial product, process, or service by trade name, trademark, manufacturer, or otherwise does not necessarily constitute or imply its endorsement, recommendation, or favoring by the United States Government or any agency thereof. The views and opinions of authors expressed herein do not necessarily state or reflect those of the United States Government or any agency thereof.

Acknowledgments

References

[1] Grierson B. 2021 Testing the DIII-D Co/counter off-axis neutral beam injected power and ability to balance injected torque *28th IAEA Fusion Energy Conf.* (Nice, France May 10–16, 2021) (Vienna: IAEA) (https://conferences.iaea.org/event/214/)

[2] Collins C. 2021 Improving fast-ion confinement and performance by reducing Alfvén eigenmodes in the $q_{\min} >$ 2, steady-state scenario *28th IAEA Fusion Energy Conf.* (Nice, France May 10–16, 2021) (Vienna: IAEA) [EX/8-2] (https://conferences.iaea.org/event/214/)

[3] Park J.-M. 2021 Off-axis neutral beam current drive for advanced tokamak *28th IAEA Fusion Energy Conf.* (Nice, France May 10–16, 2021) (Vienna: IAEA) [EX/P1-1/CN-286/1009]

[4] Chen X. 2022 Doubling off-axis electron cyclotron current drive efficiency via velocity space engineering *Nucl. Fusion* (accepted 8 Feburary 2022) (https://doi.org/10.1088/1741-4326/ac52da)

[5] Chen X. 2021 Doubling the efficiency of off-axis current drive using reactor-relevant 'top launch ECCD' on the DIII-D tokamak *28th IAEA Fusion Energy Conf.* (Nice, France May 10–16, 2021) (Vienna: IAEA) [EX/1-TH/1 H and CD and Steady-state and Operation-1] (https://conferences.iaea.org/event/214/)

[6] Barr J.A. 2021 Development and experimental qualification of novel disruption prevention techniques on DIII-D *28th IAEA Fusion Energy Conf.* (Nice, France May 10–16, 2021) (Vienna: IAEA)

[7] Du X. 2021 Experimental evidence of runaway electron tail generation via localized helical structure in pellet-triggered tokamak disruptions *Nucl. Fusion* **61** 104001

[8] Paz-Soldan C., Eidietis N.W., Liu Y.Q., Shiraki D., Boozer A.H., Hollmann E.M., Kim C.C. and Lvovskiy A. 2019 Kink instabilities of the post-disruption runaway electron beam at low safety factor *Plasma Phys. Control. Fusion* **61** 054001

[9] Paz-Soldan C. 2021 A novel path to runaway electron mitigation via current-driven kink instability *28th IAEA Fusion Energy Conf.* (Nice, France May 10–16, 2021) (Vienna: IAEA)

[10] Reux C. *et al* 2022 Physics of Runaway Electrons with shattered pellet injection at JET *Phys. Rev. Lett.* **64** 034002

[11] Reux C. *et al* 2021 Magnetohydrodynamic simulations of runaway electron beam termination in JET *Plasma Phys. Control. Fusion* **63** 035024

[12] Shiraki D. *et al* 2021 DIII-D and international research extrapolating shattered pellet performance to ITER *28th IAEA Fusion Energy Conf.* (Nice, France May 10–16, 2021) (Vienna: IAEA) [EX/5-TH/6 Disruption-2]

[13] Whyte D.G. *et al* 2003 Disruption mitigation with high-pressure noble gas injection *J. Nucl. Mater.* **313–316** 1239

[14] Hollmann E.M., Parks P.B. and Scott H.A. 2008 0D modeling of fast radiative shutdown of tokamak discharges following massive gas injection *Contrib. Plasma Phys.* **48** 260

[15] Parks P. *et al* 2017 A theoretical model for the penetration of a shattered-pellet debris plume *Theory and Simulation of Disruptions Workshop* (Princeton, NJ July 17–19, 2017) (https://pppltsdw.princeton.edu/2017-talks-presentations/)

[16] Shiraki D. *et al* 2019 Particle assimilation during shattered pellet injection *IAEA Technical Meeting on Plasma Disruptions and their Mitigation* Report INIS-XA-21M2166 (Saint-Paul-lez-Durance 20-23 Jul 2020 INIS) vol 52, p 41 (https://conferences.iaea.org/event/217/attachments/9159/12775/book-of-abstracts.pdf)

[17] Sugihara M., Shimada M., Fujieda H., Gribov Y., Ioki K., Kawano Y., Khayrutdinov R., Lukash V. and Ohmori J. 2007 Disruption scenarios, their mitigation and operation window in ITER *Nucl. Fusion* **47** 337

[18] Fitzpatrick R. 2020 Theory of edge localized mode suppression by static resonant magnetic perturbations in the DIII-D tokamak *Phys. Plasmas* **27** 042506

[19] Fitzpatrick R. and Nelson A.O. 2020 An improved theory of the response of DIII-D H-mode discharges to static resonant magnetic perturbations and its implications for the suppression of edge localized modes *Phys. Plasmas* **27** 072501

[20] Hu Q.M., Nazikian R., Grierson B.A., Logan N.C., Park J.-K., Paz-Soldan C. and Yu Q. 2019 The density dependence of edge-localized-mode suppression and pump-out by resonant magnetic perturbations in the DIII-D tokamak *Phys. Plasmas* **26** 120702

[21] Hu Q.M., Nazikian R., Grierson B.A., Logan N.C., Paz-Soldan C. and Yu Q. 2020 The role of edge resonant magnetic perturbations in edge-localized-mode suppression and density pump-out in low-collisionality DIII-D plasmas *Nucl. Fusion* **60** 076001

[22] Yu Q. and Günter S. 2011 Plasma response to externally applied resonant magnetic perturbations *Nucl. Fusion* **51** 073030

[23] Park J.-K. and Logan N.C. 2017 Self-consistent perturbed equilibrium with neoclassical toroidal torque in tokamaks *Phys. Plasmas* **24** 032505

[24] Hu Q.M. *et al* 2020 Wide operational windows of edge-localized mode suppression by resonant magnetic perturbations in the DIII-D tokamak *Phys. Rev. Lett.* **125** 045001

[25] Hu Q.M. 2021 Nonlinear two-fluid modeling of plasma response to RMPs for the ELM control in the ITER baseline *28th IAEA Fusion Energy Conf.* (Nice, France May 10–16, 2021) (Vienna: IAEA)

[26] Shafer M. *et al* 2021 Limits of RMP ELM suppression in double null *28th IAEA Fusion Energy Conf.* (Nice, France May 10–16, 2021) (Vienna: IAEA) [EX/P1-1/CN-286/930]

[27] Logan N.C. 2022 Improved particle confinement with 3D magnetic perturbations in DIII-D H-mode plasmas *Phys. Rev. Lett.* (to be submitted)

[28] Schmitz L. 2019 L–H transition trigger physics in ITER-similar plasmas with applied $n = 3$ magnetic perturbations *Nucl. Fusion* **59** 126010

[29] Kriete D.M., McKee G.R., Schmitz L., Smith D.R., Yan Z., Morton L.A. and Fonck R.J. 2020 Effect of magnetic perturbations on turbulence-flow dynamics at the L–H transition on DIII-D *Phys. Plasmas* **27** 062507

[30] Barada K. 2021 New understanding of multi-scale/multi-field pedestal turbulence, transport, and gradient behavior during type-I ELMs on the DIII-D tokamak *28th IAEA Fusion Energy Conf.* (Nice, France May 10–16, 2021) (Vienna: IAEA)

[31] Haskey S. 2021 Main-ion thermal transport in high performance DIII-D edge transport barriers *28th IAEA Fusion Energy Conf.* (Nice, France May 10–16, 2021) (Vienna: IAEA) [EX/P1-1/CN-286/750]

[32] Nelson A.O. 2021 Time-dependent experimental identification of inter-ELM microtearing modes in the tokamak edge on DIII-D *Nucl. Fusion* **61** 116038

[33] Hatch D.R. *et al* 2021 Microtearing modes as the source of magnetic fluctuations in the JET pedestal *Nucl. Fusion* **61** 036015

[34] Hassan E. 2021 Identifying the microtearing modes in the pedestal of DIII-D H-modes using gyrokinetic simulations *Nucl. Fusion* **62** 026008

[35] Chen J. 2021 Pedestal magnetic turbulence measurements in ELMy H-mode plasmas in DIII-D tokamak *28th IAEA Fusion Energy Conf.* (Nice, France May 10–16, 2021) (Vienna: IAEA) [EX/P1-1/CN-286/682]

[36] Guttenfelder W., Groebner R.J., Canik J.M., Grierson B.A., Belli E.A. and Candy J. 2021 Testing predictions of electron scale turbulent pedestal transport in two DIII-D ELMy H-modes *Nucl. Fusion* **61** 056005

[37] Schmitz L. *et al* 2021 Reducing the L–H transition power threshold via neoclassical toroidal viscosity, edge rotation reversals, and shape changes *28th IAEA Fusion Energy Conf.* (Nice, France May 10–16, 2021) (Vienna: IAEA) [EX/P1-1/CN-286/1007]

[38] Samuell C. and Mclean A.G. 2021 Advancements in understanding the 2D role of impurity radiation for dissipative divertor operation on DIII-D *28th IAEA Fusion Energy Conf.* (Nice, France May 10–16, 2021) (Vienna: IAEA) [EX/P1-1/CN-286/867]

[39] Mclean A.G. 2020 Absolute impurity concentrations during attached and detached divertor conditions in DIII-D *Bull. Am. Phys. Soc.* Bibcode: 2020APS..DPPP06003M

[40] Goldston R.J. 2012 Heuristic drift-based model of the power scrape-off width in low-gas-puff H-mode tokamaks *Nucl. Fusion* **52** 013009

[41] Goldston R.J. 2015 Theoretical aspects and practical implications of the heuristic drift SOL model *J. Nucl. Mater.* **463** 397–400

[42] Brown A.O. and Goldston R.J. 2020 Generalization of the heuristic drift SOL model for finite collisionality, and effect on flow shearing rate vs interchange growth rate *Nucl. Mater. Energy* **27** 101002

[43] Casali L., Osborne T.H., Grierson B.A., McLean A.G., Meier E.T., Ren J., Shafer M.W., Wang H. and Watkins J.G. 2020 Improved core–edge compatibility using impurity seeding in the small angle slot (SAS) divertor at DIII-D *Phys. Plasmas* **27** 062506

[44] Casali L. *et al* 2021 Improved impurity retention and pedestal performance in DIII-D closed divertor *28th IAEA Fusion Energy Conf.* (Nice, France May 10–16, 2021) (Vienna: IAEA)

[45] Nichols J. 2021 Modeling of $E \times B$ effects on tungsten redeposition and transport in the DIII-D divertor *Nucl. Fusion* accepted (https://doi.org/10.1088/1741-4326/ac14e6)

[46] Abrams T. *et al* 2021 Advances in understanding high-Z sourcing, migration, and transport on DIII-D from L-mode to high-performance regimes *28th IAEA Fusion Energy Conf.* (Nice, France May 10–16, 2021) (Vienna: IAEA) [EX/P1-1/CN-286/660]

[47] Unterberg E.A. *et al* 2020 Localized divertor leakage measurements using isotopic tungsten sources during edge-localized mode-y H-mode discharges on DIII-D *Nucl. Fusion* **60** 016028

[48] Abrams T. *et al* 2019 Impact of ELM control techniques on tungsten sputtering in the DIII-D divertor and extrapolations to ITER *Phys. Plasmas* **26** 062504

[49] Abrams T. *et al* 2018 Experimental validation of a model for particle recycling and tungsten erosion during ELMs in the DIII-D divertor *Nucl. Mater. Energy* **17** 164–73

[50] Wang L. 2021 Achievements of actively controlled divertor detachment compatible with sustained high confinement core in DIII-D and EAST *28th IAEA Fusion Energy Conf.* (Nice, France May 10–16, 2021) (Vienna: IAEA)

[51] Ding S. 2021 A low plasma current (∼8 MA) approach for ITER's $Q = 10$ goal *28th IAEA Fusion Energy Conf.* (Nice, France May 10–16, 2021) (Vienna: IAEA)

[52] Wang L. *et al* 2021 Integration of full divertor detachment with improved core confinement for tokamak fusion plasmas *Nat. Commun.* **12** 1365

[53] Wang H.Q. *et al* 2021 Observation of fully detached divertor integrated with improved core confinement for tokamak fusion plasmas *Phys. Plasmas* **28** 052507

[54] Ding S., Jian X., Garofalo A.M., Yan Z., McClenaghan J., Guo W. and Grierson B.A. 2020 The dominant microturbulence instabilities in the lower q_{95} high β_p plasmas on DIII-D and predict first extrapolation *Nucl. Fusion* **60** 016023

[55] Snyder P.B. *et al* 2015 Super H-mode: theoretical prediction and initial observations of a new high performance regime for tokamak operation *Nucl. Fusion* **55** 083026

[56] Snyder P.B. *et al* 2019 High fusion performance in super H-mode experiments on alcator C-mod and DIII-D *Nucl. Fusion* **59** 086017

[57] Knolker M. *et al* 2020 Optimizing the super H-mode pedestal to improve performance and facilitate divertor integration *Phys. Plasmas* **27** 102506

[58] Wilks T. 2021 Development of an integrated core–edge scenario using the super H-mode compatible with JET and ITER operation *28th IAEA Fusion Energy Conf.* (Nice, France May 10–16, 2021) (Vienna: IAEA)

[59] Snyder P.B., Groebner R.J., Hughes J.W., Osborne T.H., Beurskens M., Leonard A.W., Wilson H.R. and Xu X.Q. 2011 A first-principles predictive model of the pedestal height and width: development, testing and ITER optimization with the EPED model *Nucl. Fusion* **51** 103016

[60] Knolker M. *et al* 2021 On the stability and stationarity of the super H-mode combined with an ion transport barrier in the core *Plasma Phys. Control. Fusion* **63** 025017

[61] Eldon D. *et al* 2021 An analysis of controlled detachment by seeding various impurity species in high performance scenarios on DIII-D and EAST *Nucl. Mater. Energy* **27** 100963

[62] Laggner F.M. *et al* 2020 Real-time pedestal optimization and ELM control with 3D fields and gas flows on DIII-D *Nucl. Fusion* **60** 076004

[63] Petty C.C. 2021 New regime for high-beta hybrid using off-axis current drive on DIII-D *28th IAEA Fusion Energy Conf.* (Nice, France May 10–16, 2021) (Vienna: IAEA)

[64] Petrie T.W. *et al* 2019 High-performance double-null plasmas under radiating mantle scenarios on DIII-D *Nucl. Mater. Energy* **19** 267

[65] Hanson J. 2020 Resistive contributions to the stability of DIII-D ITER baseline demonstration discharges *Phys. Plasmas* **28** 042502

[66] Austin M.E. *et al* 2019 Achievement of reactor-relevant high normalized beta and high confinement with L mode edge in negative triangularity shape in DIII-D *Phys. Rev. Lett.* **122** 115001

[67] Marinoni A. *et al* 2019 H-mode grade confinement in L-mode edge plasmas at negative triangularity on DIII-D *Phys. Plasmas* **26** 042515

[68] Marinoni A. 2021 Diverted negative triangularity plasmas on DIII-D: the benefit of high confinement without the liability of an edge pedestal *28th IAEA Fusion Energy Conf.* (Nice, France May 10–16, 2021) (Vienna: IAEA)

[69] Saarelma S. 2021 Ballooning instability preventing the H-mode access in plasmas with negative triangularity shape on the DIII-D tokamak *Plasma Phys. Control. Fusion* (https://doi.org/10.1088/1361-6587/ac1ea4)

[70] Buttery R.J. 2019 DIII-D research to prepare for steady state advanced tokamak power plants *J. Fusion Energy* **38** 72–111

[71] Prater R., Moeller C.P., Pinsker R.I., Porkolab M., Meneghini O. and Vdovin V.L. 2014 Application of very high harmonic fast waves for off-axis current drive in the DIII-D and FNSF-AT tokamaks *Nucl. Fusion* **54** 083024

[72] Lau C., Jaeger E.F., Bertelli N., Berry L.A., Green D.L., Murakami M., Park J.M., Pinsker R.I. and Prater R. 2018 AORSA full wave calculations of helicon waves in DIII-D and ITER *Nucl. Fusion* **58** 066004

[73] Pinsker R.I. 2015 Whistlers, helicons, and lower hybrid waves: the physics of radio frequency wave propagation and absorption for current drive via Landau damping *Phys. Plasmas* **22** 090901

[74] Wukitch S.J., Shiraiwa S., Wallace G.M., Bonoli P.T., Holcomb C. and Pinsker R.I. 2017 High field side lower hybrid current drive simulations for off-axis current drive in DIII-D *EPJ Web Conf.* **157** 02012

[75] Garofalo A.M. *et al* 2006 Access to sustained high-beta with internal transport barrier and negative central magnetic shear in DIII-D *Phys. Plasmas* **13** 056110

[76] Van Compernolle B. 2021 The high-power helicon program at DIII-D: gearing up for first experiments *28th IAEA Fusion Energy Conf.* (Nice, France May 10–16, 2021) (Vienna: IAEA)

[77] Wukitch S. 2019 DIII-D high field side lower hybrid current drive: experiment overview *46th European Physical Society Conf. on Plasma Physics* (Milan, Italy July 8–12, 2019) (https://www.epsplasma2019.eu/)

[78] Wang H.-Q. *et al* 2021 The effect of synergy between divertor geometry and drifts on divertor power dissipation in the DIII-D small angle slot divertor *28th IAEA Fusion Energy Conf.* (Nice, France May 10–16, 2021) (Vienna: IAEA) [EX/P2-2/CN-286/1499]

[79] Weisberg D.B., Paz-Soldan C., Liu Y.Q. and Logan N.C. 2019 Optimizing multi-modal, non-axisymmetric plasma response metrics with additional coil rows on DIII-D *Nucl. Fusion* **59** 086060

[80] Weisberg D. 2021 Passive deconfinement of runaway electrons using an in-vessel helical coil *Nucl. Fusion* **61** 106033